Marine and Petroleum Geology 134 (2021) 105348

Contents lists available at ScienceDirect

Marine and Petroleum Geology

journal homepage: www.elsevier.com/locate/marpetgeo

Multi-scale pore structural change across a paleodepositional transition in Utica shale probed by gas sorption overcondensation and scanning

Eleanor G. Pitcher [a,b], David J. Large [a], Robin S. Fletcher [c], Sean P. Rigby [a,b,*]

[a] Department of Chemical and Environmental Engineering, University of Nottingham, University Park, Nottingham, NG7 2RD, UK
[b] Geo-energy Research Centre, University of Nottingham, University Park, Nottingham, NG7 2RD, UK
[c] Johnson Matthey, P.O. Box 1, Belasis Avenue, Billingham, Cleveland, TS23 1LB, UK

ARTICLE INFO

Keywords:
Depositional transition
Pore network
Advanced adsorption
Mercury porosimetry
Computerised X-ray tomography
SEM
Scanning loops
Bulk condensation

ABSTRACT

Pore structure and network configuration in shales greatly impacts physical processes important for hydrocarbon migration, methane extraction, gas storage, or carbon sequestration. The multi-scale nature of the porosity in shales presents significant challenges to its comprehensive and accurate characterisation. The under-used gas overcondensation technique can bridge characterisation of micropores, below the detection limit of mercury porosimetry and many imaging methods, to that of macroporosity undetected by conventional adsorption experiments. Further, gas sorption scanning curves revealed advanced condensation effects that allowed the probing of the inter-relation and juxtaposition of multi-scale porosities. It was found that the changeover period, from primarily clay to carbonaceous deposits in the Utica shale, was associated with growth in the disorder of the pore network over particular key length-scales highlighted by percolation processes in the gas overcondensation and scanning curves. Critical path theory suggests that the marked percolation knee that developed in overcondensation data at the depositional transition would identify a particular pore size that is characteristic of the wider network, and would control mass transport. The peak in pore network disorder was also associated with a peak in total organic carbon content and the accessible porosity was shown to be dominated by the organic carbon phase. Complementary mercury porosimetry combined with computerised X-ray tomography has shown substantial changes in the type, and super-micron-scale spatial distribution, of the nanoporosity down to approximately 3 nm, accessible to mercury, across the depositional transition, probably related to the amount and disposition of carbonate minerals.

1. Introduction

1.1. Background

Improved knowledge concerning shale rocks is important because of their involvement in oil and gas production, gas storage, carbon dioxide sequestration, radioactive waste repositories, and civil engineering (Kim et al., 2017; Liu et al., 2019; Jarvie et al., 2005). Understanding the pore structure of shale rocks is necessary to predict gas storage, mass transport and geomechanical properties (Spanakos and Rigby, 2020). However, the void-space structure of shales is complex and multi-scale, with voids ranging in size from macroscopic faults and fractures down to atomic-scale gaps between clay layers. Further, the composition and surface chemistry of shales is also similarly complex. This multi-scale complexity presents a challenge to pore structure characterisation which necessitates the development of new methodologies and techniques. In particular, it is necessary to know how structures on different scales are juxtaposed relative to each other.

Imaging methods, such as computerised X-ray tomography (CXT), focussed ion beam scanning electron microscopy (FIB-SEM), and electron tomography (3D transmission electron microscopy) can be used to visualise void spaces more directly in three dimensions (Rigby, 2020). However, strictly, this is using computer reconstructions that can be subject to artefacts. Further, imaging data-sets require filtering, to remove noise to make void-solid interfaces more visible, and then segmentation to identify void and solid phases, which both involve subjective elements. In addition, the combinations of fields of view and resolutions currently feasible mean that one imaging method alone cannot study the whole range of length-scales of pores present in shales. For example, Keller et al. (2013) performed representative volume

* Corresponding author. Department of Chemical and Environmental Engineering, University of Nottingham, University Park, Nottingham, NG7 2RD, UK.
E-mail address: sean.rigby@nottingham.ac.uk (S.P. Rigby).

https://doi.org/10.1016/j.marpetgeo.2021.105348
Received 7 December 2020; Received in revised form 10 September 2021; Accepted 24 September 2021
Available online 27 September 2021

calculations that showed FIB-SEM sample volumes of a maximum of several hundred microns cubed were smaller than the representative length-scale cut-off and many of the structural heterogeneities present in the sample studied. It is simply not possible to use imaging modalities with the finest resolution to study statistically meaningful volumes of a sample with multi-scale heterogeneity and pores.

Hence, multi-scale methodologies, utilising two or more imaging modalities, that can together span much of the requisite length-scale range have been proposed by workers such as Keller et al. (2013), Ma et al.(2017, 2019), and Saif et al. (2017). However, given the sample volume limitations at the highest resolution, some sort of scale-up method is required. This often means identifying and classifying a small number (approximately 1–10) of characteristic phases (for example organic material or quartz minerals) that are assumed to possess identical parameters for all instances over the larger length-scales. This means the requirement to study a representative sub-set of regions identified as each phase at smaller length-scales to obtain the class-specific characteristic parameters. There are a number of issues with this approach since it requires, often subjective, identifications of regions as belonging to a particular phase. Further, it requires knowledge of how many examples of regions of a particular phase need to be examined to get properly representative parameters for the class as a whole. There are also complications when individual micro-scale grains making up a larger composite are smaller than the correlation length for the materials from which they are made (Nepryahin et al., 2016a).

Alternatively, indirect methods, such as mercury porosimetry, have been used to establish the relative disposition of void-space features observed in images obtained at different length-scales (Hemes et al., 2015). Such a different approach to multi-scale imaging and upscaling for studying structure-transport relationships in multi-scale porosity is to use a filtering type approach (Rigby, 2020). In the filtering approach a particular sub-set of a much more complex overall network is isolated or knocked-out, and the impact of this on the process of interest, such as mass transport, is examined. For example, using mercury porosimetry scanning curves, pores of progressively smaller size can be removed by mercury entrapment, and the impact of doing so on mass transport assessed via the rate of adsorption of gas before and afterwards (Nepryahin et al., 2016a,b; Rigby et al., 2020). Alternatively, NMR cryodiffusometry can be used to isolate the behaviour of a particular sub-set of pores within a much larger network. However, there are lower limits on the pore sizes that can be probed by mercury porosimetry and cryoporometry.

1.2. Gas sorption overcondensation and scanning

Conventional gas sorption experiments are one of the very few techniques that can be used to study the pore structure of shales, down to the very smallest molecular-scale (<2 nm) porosity below the resolution limit of many imaging techniques (Rigby, 2020). However, in previous work (eg Wang et al., 2018; Sang et al., 2020), the type of gas sorption experiment conducted was such that the data typically consisted just of a boundary adsorption isotherm up to a limited ultimate pressure, followed by a pseudo-boundary desorption isotherm, that is often really just an unrecognised descending scanning curve because complete pore-filling with condensate was not achieved at the top (high-pressure end) of the adsorption isotherm. Hence, conventional gas sorption alone cannot cover the complete pore size range, including macropores, nor deliver information on the inter-relationship between pores over a much wider length-scale range.

However, more comprehensive, and much richer, data-sets can be obtained for shales using overcondensation and sorption hysteresis scanning curves techniques. The upper cut-off in pore size that can be studied with gas sorption is limited by the highest ultimate pressure obtained in the experiment. This is often truncated well before saturation to avoid flooding the apparatus with bulk condensate. However, the overcondensation method allows the full boundary desorption isotherm to be obtained even for samples where complete pore-filling is not achieved at the top of the adsorption isotherm during conventional experiments (Aukett and Jessop, 1996; Murray et al., 1999). This technique was used to show that conventional gas sorption experiments only indirectly detected the macroporosity generated by thermochemical treatment of Rempstone shale from the UK (Rigby et al., 2020). In the overcondensation experiments a separate, both high and wide, hysteresis loop was obtained above and beyond that seen in conventional experiments.

Gas sorption scanning experiments enable the spatial inter-relationship between different pore sizes to be determined (Esparza et al., 2004). Sorption hysteresis scanning involves construction of isotherm curves or loops by truncating a series of pressure increments or decrements before they reach the upper or lower hysteresis closure points (Tompsett et al., 2005). As implicitly mentioned above, the simplest type of scanning experiment is a descending scanning curve originating from the boundary adsorption curve created by reversing the direction of pressure step changes before achieving complete pore-filling with condensate (at the Gurvitsch volume). The descending scanning curve can be converted into a scanning loop by once more changing the direction of the pressure step changes, before the descending scanning curve reaches the lower hysteresis closure point, thereby giving rise to an ascending branch in addition to the descending branch. The ascending branch of the loop will then re-join the boundary adsorption isotherm. An ascending scanning curve can also be created springing from the boundary desorption isotherm by changing from pressure decrements to increments part way down the boundary desorption isotherm. This ascending scanning curve can be converted into a scanning loop by again changing the direction of pressure changes, but from increases to decreases, before the ascending curve reaches the boundary adsorption isotherm. Scanning curves and loops can take a variety of forms and shapes which contain information on the nature of the phase transitions of the adsorbate and pore structure of the adsorbent, as will be described below.

In the past, only very limited use has been made of gas sorption scanning curves and loops to study shales. Seemann et al. (2017) measured a small series of descending water sorption scanning curves for Sichuan 211 shale rock. These curves all converged on the lower hysteresis closure point (or thereabouts, as there was some slight low pressure hysteresis). Very limited analysis was conducted of these curves. Barsotti et al. (2020) measured scanning curves for n-butane and n-pentane for Middle Eastern gas shales. In both cases, crossing scanning curves were obtained. The interpretation of these data was limited to noting that crossing scanning curves are most often associated with more ordered, templated silica materials, and suggesting that the form of the adsorption isotherm was controlled by pore morphology, and that of the desorption by cavitation. Rigby et al. (2020) also observed crossing behaviour in ascending scanning curves springing from the boundary desorption isotherm obtained, for a thermochemically treated shale sample, using the aforementioned overcondensation method. This form of the scanning curve, together with the aforementioned wide hysteresis of the overcondensation desorption, was consistent with a void space consisting of large pore bodies shielded by narrow pore windows. From SEM studies, it was observed that the thermochemical treatment of the shale had created ovoid, bubble-like pore bodies, that intersected at circular windows, within the organic/carbon component of the shale, that would give rise to the type of scanning curve behaviour described by Rigby et al. (2020). This type of intersecting ovoid pore has also been observed within organic material for a variety of natural shale samples, including marine Longmaxi shales (Chen et al., 2019; Ji et al., 2019), Upper Permian marine-terrestrial transition Longtan Formation shales, and Horn River shale (Curtis et al., 2012).

Gas sorption scanning experiments can be used to bridge between sample particle scale and nanometre-scale characterisations of complex multiscale porous media. This is because, while the particular pressure

at which basic physical processes, such as capillary condensation, arises is controlled by nano-scale characteristics, such as pore size, the pore-to-pore co-operative effects, such as advanced condensation/adsorption (also known as the 'cascade effect'), network delayed condensation, and pore-blocking, present for complex pore networks operate over length-scales from the neighbouring pore up to the size of the sample particle itself (Rigby, 2018, 2020). These pore-to-pore co-operative effects control the overall shape of the gas sorption scanning curves through their dependencies on the spatial disposition of the pore size distribution and network connectivity. The overall size of the scanning curve or loop is very often related to the volume of sample that the underlying physical processes are affecting. For example, the shape of the boundary desorption isotherm around the percolation knee generally relates to the formation of sample-spanning clusters of emptied pores (Seaton, 1991; Rigby et al., 2004). The critical pore size controlling desorption for a given set of pores may be a macroscopic (>10 μm) distance away. The pore-to-pore co-operative process of percolation during gas desorption sifts out the particular pore size at the knee, and, thereby, identifies the rate-limiting pore size, according to critical path analysis theory (Katz and Thompson, 1986; Ambegaokar et al., 1991; Seaton et al.., 1997), for Knudsen diffusion or permeation of gas moving from the given pores to the exterior (or vice-versa).

1.3. Hybrid mercury porosimetry and X-ray imaging method

An alternative, complementary technique for studying the macro-/micro-scale spatial disposition of the nanoscopic pore structure is the combination of liquid metal (such as mercury or Wood's metal) intrusion with electron microscopy and/or computerised X-ray tomography (CXT) (Cody and Davis, 1991; Ruffino et al., 2001; Nepryahin et al., 2016a; Kauffmann, 2010). The variable intrusion pressure employed defines a lower limit to the pore sizes that can be penetrated, and the entrapped metal acts as a tracer for where the metal has managed to reach at that pressure thus revealing the spatial disposition of regions of void space accessible via particular pore neck sizes. The imaging also reveals whether the liquid metal has actually intruded rather than only seemingly to have done so due to pore collapse under the pressures used.

Some workers (eg Garum et al., 2020) have suggested that mercury porosimetry should not be used with shales due to the high pressures involved leading to crushing of the sample. However, apparent anomalies in pore size distributions (PSDs) leading to the suggestion of crushing can arise because the wrong data analysis method is used for converting raw data from porosimetry, and from independent comparison data, such as gas sorption, to PSDs. For example, for mercury porosimetry, correctly calibrated contact angle and surface tension parameters are needed (Kloubek, 1981). In addition, gas overcondensation allows the comparison of PSDs from mercury intrusion and gas desorption even for macropores, and there is no issue for gas overcondensation of confusing multi-layer adsorption with capillary condensation in unfilled macropores, as there is for conventional sorption experiments (Gregg and Sing, 1982). Given gas desorption and mercury intrusion are both invasion percolation processes then they should give rise to identical PSDs.

1.4. Structure of paper

In this work nitrogen sorption overcondensation and scanning loop methods will be used to probe the changes in the void space structure resulting from a paleodepositional (mineralogical) transition within Utica shale. Scanning loop data will be used to assess the relative changes in the spatial juxtaposition and connectivity of components of the void space for a series of Utica shale rock core samples of increasing depth. It will be seen that scanning loops provide a rich data-source linking information on both the nanoscopic and macroscopic changes in the void space across the transition. Complementary SEM and CXT imaging, and mercury porosimetry will be used to support the interpretation of the gas sorption data, and reveal the evolution in the macro-/micro-scale spatial disposition of accessible nanopore necks larger than approximately 3 nm across the paleodepositional transition.

2. Theory

2.1. Gas sorption

Natural rock surfaces are often rough on the molecular scale. This roughness is neglected in conventional models of gas sorption, such as the standard Brunauer-Emmett-Teller (BET) equation (Rouquerol et al., 1999). Concavities in the surface mean that the space for adsorbing the second and subsequent layers of an adsorption multi-layer declines with distance from the surface, and the maximum molecular capacity of each successive layer decreases. For surfaces that exhibit the particular property of self-similarity over several length-scales, and are, thus, fractals, the decrease in the capacity of each layer of adsorbate is given by the equation (Pfeifer and Avnir, 1983):

$$\frac{A_i}{A_1} = i^{2-d} \tag{1}$$

where A_1 is the area in the first adsorbed layer, A_i is the area in the ith adsorbed layer, and d is the surface fractal dimension ($2 \leq d \leq 3$). This effect can be incorporated into the standard BET model such that a fractal version thereof is obtained. This is given by (Mahnke and Mögel, 2003):

$$log(V) = log(V_m) + log\left[\frac{Cx}{1-x+Cx}\right] - (3-d)log(1-x), \tag{2}$$

where V is the amount adsorbed, V_m is the monolayer capacity, C is the BET constant, and x is the relative pressure. The effect of the fractal roughness, as described by Equation (1), is to lead to a decline in the amount adsorbed in each successive layer of adsorbate.

Rocks are complex mixtures of different minerals. The homotattic (meaning isoenergetic) patch model was introduced in order to account for the impact on adsorption of the chemical heterogeneity of such surfaces (Walker and Zettlemoyer, 1948). This model considers the surface of the adsorbent to consist of a patchwork of different types of site, perhaps corresponding to different mineral grains, each with their own characteristic adsorption behaviour. The model assumes that each of these patches is large, such that edge effects, where they neighbour other patches, are negligible. The resulting overall adsorption is thus a composite of the behaviour of the set of patches, such that:

$$V = V_m(p_1 I_1 + p_2 I_2 + \ldots + p_i I_i + \ldots), \tag{3}$$

where I_i is the isotherm equation describing adsorption on the ith patch, and p_i is the fraction of the surface occupied by patches of type I_i, such that the various p_i-values obey:

$$p_1 + p_2 + \ldots + p_i + \ldots = 1. \tag{4}$$

The homotattic patch is based on the understanding that different materials will have different sorption behaviours based on their surface chemistry. Shales have a very heterogeneous surface formed of organic and inorganic minerals. In this work, the homotattic patch theory will be used to separate the contributions to adsorption from each of the organic and inorganic matter phases in the shale. The homotattic patch models used represented adsorption on the inorganic phase using the fractal BET equation, or the BET equation with a finite number of adsorbed layers (n) in the multilayer, while the organic phase was represented by an empirical fit to an experimental isotherm for a pure organic matter sample (kerogen) extracted by acid-dissolution of the inorganic matrix given by:

The experimental isotherm data was fitted only over the relative pressure (x) range of $0< x < 0.8$, since the BET models are only for the multi-layer adsorption process, and do not account for the effects of surface tension in capillary condensation. Hence, the resultant fitted homotattic patch models are:

$$\left[\sum_{x>0}^{x\leq 0.025} 6.8705\cdot\ln(x)+92.807\right]+\left[\sum_{x>0.025}^{x\leq 0.7} -34.08x^2+110.81x+76.7\right]+\left[\sum_{x>0.7}^{x\leq 0.925} 56.209e^{1.2458x}\right]+\left[\sum_{x>0.925}^{x\leq 1} 67470x^2-128284x+61174\right] \quad (5)$$

$$V=\sum_{x=0}^{x=0.8}(1-p)\cdot kerogen+p\cdot V_m\frac{Cx}{1+x(C-1)}(1-x)^{-(3-d)} \quad (6)$$

including the fractal BET equation, and:

$$V=\sum_{x=0}^{x=0.8}(1-p)\cdot kerogen+p\cdot V_m\cdot\frac{C}{\frac{1}{x}-1}\cdot\frac{[1-(n+1)x^n+nx^{n+1}]}{[1+(C-1)x-cx^{n+1}]} \quad (7)$$

including the finite multilayer BET equation.

Capillary condensation in larger pores is predicted by the Kelvin equation (Gregg and Sing, 1982):

$$ln\left(\frac{P}{P_0}\right)=\frac{-k\gamma V_M cos\theta}{RT(r_p-t)}, \quad (8)$$

where P/P_0 is the relative pressure at which condensation occurs in a cylindrical pore of radius r_p, t is the multilayer thickness, k is a geometry parameter and depends on the pore type (for a cylindrical pore open at both ends $k=1$; and for a pore with one dead end, or for desorption from a hemi-spherical meniscus, $k=2$), γ is the surface tension and V_m is the molar volume of the condensed liquid phase, θ is the contact angle with which the liquid meets the wall, and T is the absolute temperature. In small pores, with a high radius of surface curvature, the multilayer, or t-layer, thickness will be greater than for large pores. Broekhoff and de Boer (BdB) (1967, 1968) have provided equations for the thickness of the t-layer for adsorption and desorption processes in small pores, which will be used to determine pore sizes for the scanning loops in this work. This is because there is some indication it gives rise to the correct hysteresis width for 3D inter-connected, disordered silica pore networks (Hitchcock et al., 2014).

It is noted from Equation (8) that capillary condensation will occur earlier (lower pressure) for a hemispherical meniscus compared to a cylindrical sleeve-shaped meniscus. This can lead to the operation of a pore-to-pore co-operative adsorption process within pores of underlying geometries akin to the so-called through ink-bottle arrangement (Rigby, 2018, 2020). For a regular, through ink-bottle pore geometry, access to a larger diameter pore body is only through smaller diameter pore necks (or windows) that are located at the two ends of, and are co-axial with, the pore body. Pore-filling during adsorption in such a system is initiated by condensation via cylindrical-sleeve shaped menisci in the necks. The filling of the pore necks completes the hemispherical menisci located at the ends of the pore body, meaning condensation in the body can be initiated from them, before that from the cylindrical-sleeve shaped meniscus along the length of the pore wall. Hence, the pore necks adjoining the pore body can co-operate in lowering the filling pressure for the latter. The ink-bottle pore model can also illustrate the pore-to-pore co-operative effect known as pore-blocking or pore-shielding that can occur during desorption. Evaporation of the condensate from a pore can only occur when the pressure drops below the critical value given by the Kelvin equation if there is a free meniscus with the vapour phase. In the case of the pore body in the ink-bottle, when the external vapour pressure drops below the critical value to destabilise the condensate in it, there is no free meniscus because the condensate in the necks is still above its critical pressure. The liquid in the pore body thus enters a metastable liquid state until the pressure is reduced sufficiently for the liquid in the necks to evaporate. Then the meniscus will advance to the junction of the neck and body and the metastable liquid in the body can finally evaporate.

These pore-to-pore co-operative effects will also operate in much more complex, disordered networks consisting of many more inter-connected pores. The advance of condensate or vapour phase through the network, upon pressure changes one way or another, is controlled by the numbers of different pathways possible, which, in turn, depends upon the overall size and connectivity of the pore network (Shiko et al., 2012). This network penetration process for highly disordered systems can be analysed using percolation theory, which is explained in more detail elsewhere (Seaton, 1991).

3. Materials and methods

3.1. Sample collection and geological setting

Samples were collected from the Upper Ordovician Utica and Point Pleasant Formations, which are major shale gas plays, in the Appalachian Basin (Colton, 1961; Brinkley, 2016; Sweda, 2019). The Utica shale accumulated in this deepening foreland basin (Colton, 1961; Sweda, 2019). Deposition of this transgressive sequence (Wickstrom, 2013) is characterised by the transition from shallow marine carbonates of the Point Pleasant Formation to siliciclastic mudstones of the Utica Formation (Patchman and Carter, 2015), with the transition between formations marked by generally elevated total organic carbon (TOC) concentrations (Hickman et al., 2015). Samples were taken across this transition to enable characterisation and comparison of carbonate-rich, clay-rich and high concentration TOC lithotypes.

Samples were collected from a 22 cm diameter core taken from a borehole located in Portage County, eastern Ohio (Well: Port 2 A HSU, Location: Lat: 41.10299 N, Long: 81.25678 W). The series of samples used in this work, denoted U1-5, were collected at regular intervals through the formations at borehole depths of between 5800 and 6106 ft. Photographs of the core samples are included in Appendix 1. Samples U1 and U2 are from the Utica Formation, U3 is from the base of the Utica Formation where it transitions to the lower Point Pleasant Formation, and samples U4 and U5 represent the lower Point Pleasant Formation.

The Utica Formation samples are fine grained light to dark grey calcareous mudstones. As the depth decreases the quantity of carbonates also decreases resulting in reduced evidence of bioturbation and more clearly defined laminations. The underlying Point Pleasant Formation samples U4-5 are calcareous grey mudstone with abundant thin 0.5–4 cm interbedded light grey limestone.

3.2. Nitrogen sorption and overcondensation

The conventional nitrogen adsorption/desorption isotherms were measured at liquid nitrogen temperature (77 K) using a Micromeritics ASAP 2020 physisorption analyser. Measurements were taken over the relative pressure (P/Po) range of 0.01–0.995 for adsorption and desorption from 0.995 to 0.10 P/Po. The equilibration times used were 20 s and 60 s. Two different times were tested to ensure that the sample isotherm was fully equilibrated. The samples were outgassed at 140 °C for 2 h under vacuum prior to analysis.

The overcondensation experiments were carried out on a Micromeritics ASAP 2020 physisorption analyser using a method similar to that described by Murray et al. (1999). In the overcondensation experiment, the first stage is to increase the pressure in the sample tube to higher than the saturated vapour pressure of nitrogen. This pressure increase should facilitate sufficient condensation such that even the biggest pores are filled with liquid nitrogen at the start of the overcondensation desorption isotherm, which will probably inevitably also involve some bulk condensation in the sample tube. This bulk condensation is what is avoided in the conventional experiment. The required period to reach this stage is dependent upon the sample size and the pore volume. While it does not matter if the volume of condensate is much higher than that needed for complete pore filling, the total duration of the experiment would be much longer in that case. Once complete pore-filling had been achieved, the pressure was lowered to just below the saturated vapour pressure of nitrogen such that the bulk condensate vaporized completely while keeping all the sample internal porosity liquid-filled. Once this stage has been accomplished, the first data point on the overcondensation desorption isotherm can be measured. This point corresponds to the total pore volume of the sample. The pressure is then progressively lowered in small steps, and the rest of the desorption isotherm was obtained in the usual way.

3.3. Mercury porosimetry

Samples were oven dried overnight at 100.0 °C in order to remove any pore water that may be present within the sample. Once dried, samples were prepared for mercury intrusion porosimetry (MIP) where they underwent low- and high-pressure analysis at ambient temperature and constant volume. Low-pressure analysis was carried out up to 0.207 MPa (30 psia), and high-pressure to 414 MPa (60,000 psia) on a Micromeritics AutoPore IV 9500, before mercury was extruded and the system returned to ambient pressure.

3.4. Computerised X-ray tomography (CXT)

Following mercury porosimetry, CXT was carried out on an Xradia Versa XRM-500. The Xradia Versa XRM-500 is a high-resolution 3D X-ray CT system capable of submicron resolution. The samples were scanned with source parameters 140 kV and 71 μA with a resulting pixel size of 6.7997 μm.

3.5. Scanning electron microscopy (SEM) and mineral liberation analysis (MLA)

SEM MLA was carried out on an FEI Quanta 600 (operated at 20 kV, working distance of 13 mm and spot size 7) equipped with mineral liberation analysis software which enables the quantification of sample mineralogy by taking several energy dispersive X-ray (EDX) points. The analysis used combined EDS software by BRUKER and Mineral Liberation Analysis (MLA) software by JKTech/FEI that allows automated large area analysis of polished specimens to identify and quantify mineral composition and distribution. The EDX points were associated with a specific dispersive X-ray spectrum which could be matched to known (from a mineral database) minerals. There are several identification and quantification techniques that can be carried out in order to establish mineral phases within the sample. This identification allowed the modal mineralogy (area % of the sample) to be calculated by the computer software (Sylvester, 2012).

After the acquisition of the backscattered electron (BSE) SEM image several processing steps are taken before producing the mineral map and modal mineralogy for the sample. The processing steps that needed to be carried out are de-agglomeration/segmentation of chips, phase segmentation of minerals, and mineral identification by X-ray analysis of the EDX points. Particles were de-agglomerated to remove potential bias where grains may be touching and mineral fractions in contact with each other which would not usually be so. Phase segmentation was carried out to maximise the contrast in grey-scale between minerals so that phase boundaries were defined as clearly as is possible; doing this enables mineral phases to be picked out in different grey-scales, with lighter elements appearing darker and heavier elements appearing brighter. Mineral identification was carried out by matching the EDX point data from SEM to a known mineral database; artificial colours were associated to minerals and the process repeated until all possible minerals are identified (Sylvester, 2012).

MLA was carried out on each defined grey-scale mineral phase to produce an X-ray image which is compared to a mineral list. Where mineral phases are not clearly defined, a point measurement was used to define them as one or another, and not separate the phases. In this case an area X-ray analysis was performed which rastered over a given area to determine the two or more mineral phases in the section and was thereby able to separate them. For X-ray mapping a grid was imposed on the sample and at each grid point an X-ray spectrum was collected. At this level of detail, the separate mineral phases can be resolved (Fandrich et al., 2007). After this processing there is still often a significant amount of so-called unknowns which can be resolved by picking spots, lines or areas of the SEM image to generate an X-ray spectrum. The result of this is that, if the mineral phases are not well separated (clays), mixed phase analyses are collected.

In order to perform SEM experiments, samples were embedded in epoxy resin in different orientations, i.e. parallel and perpendicular to the bedding plane. They were placed in a vacuum oven until the air bubbles were removed from the samples and left to set overnight. These were then polished with decreasing coarseness of polishing pads in order to expose the sample and produce a smooth surface in order to obtain the best energy dispersive X-ray analysis. Before analysis occurs, samples are carbon coated in a 10–20 nm thick coat of carbon.

Scanning electron microscopy (SEM) allows areas of approximately 1 cm–5 μm to be viewed and features at a scale of 50–100 nm to be seen (Swapp, 2017). This means it is not a good technique to determine complete PSDs, that include microporosity and molecular-scale pores, but is a good technique to establish mineralogy and mineral distributions in the sample.

3.6. Total organic carbon (TOC) evaluation

RockEval pyrolysis was carried out by the British Geological Survey (Keyworth, U.K.). This technique is used to determine the hydrocarbon generation potential of rocks, the type of organic matter, and the maturity thereof. The standard experimental procedure used involved heating the sample in nitrogen, and using flame ionisation detection to detect and quantify the hydrocarbonaceous products. During this process the S1 peak is determined by heating up to 300 °C, which corresponds to free hydrocarbons (gas and oil); the S2 peak is determined by continued heating between 300 and 650 °C and represents the hydrocarbons generated by organic matter cracking. The S3 peak is derived during the cooling period after the S2 peak has been established and corresponds to the quantity of carbon dioxide within the sample. After the pyrolysis in nitrogen was completed the residual organic and inorganic carbon content was pyrolysed by combustion in air from 300 to 850 °C. By establishing these parameters, the total organic carbon content (TOC %) was calculated as the sum of the pyrolysed organic content and residual organic content.

4. Results

4.1. Sample petrology

As seen from Fig. 1, the major mineral composition of the samples, as determined using MLA, varies as expected with the Point Pleasant Formation samples U4 and U5 enriched in carbonate and the Utica Formation samples (U1, U2) enriched in clay. Examples of images, and the

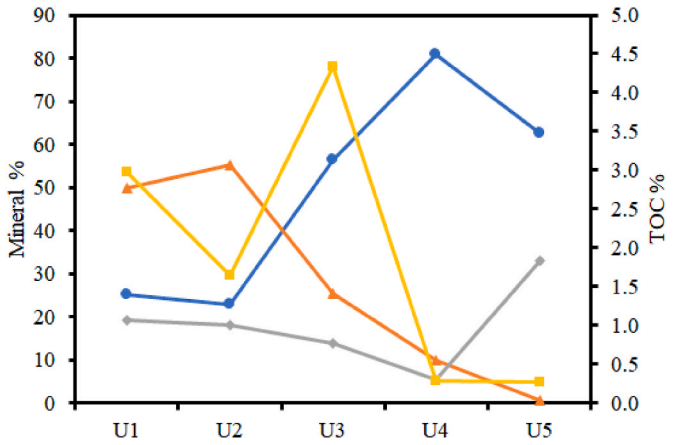

Fig. 1. Variation of mineral composition (carbonates (calcite and dolomite), blue circles; clays (illite, kaolinite and goethite), orange triangles; silicates (quartz, muscovite and albite), grey diamonds) and TOC (yellow squares)) for the series of Utica shale samples U1 to U5. The lines shown are to guide the eye to the trends in composition across the series of samples. (For interpretation of the references to colour in this figure legend, the reader is referred to the Web version of this article.)

full mineralogy, from SEM-MLA analysis are given in Appendix 2. The Utica Formation ranges from 25 to 59% illite content, while the corresponding values for the Point-Pleasant Formation are 0.5–10%. Less than 1% kaolinite was observed in all samples and any other clay fractions were too small to resolve. Carbonate minerals identified are calcite and dolomite, with the latter associated with localised fracturing. In the Utica Formation carbonates makes up 15–56% with no dolomite. In the Point Pleasant formation carbonates make up 63–80%, with 2% and 10% dolomite observed only in samples U5 and U4, respectively. The silicates present in the samples are primarily quartz and muscovite with some small quantities of albite identified. For the Utica Formation, silicates comprise 13–20% and the corresponding values are 5–33% for the Point Pleasant Formation. Several sulphides and oxides were also identified, but these do not contribute more than 2% in any sample when combined.

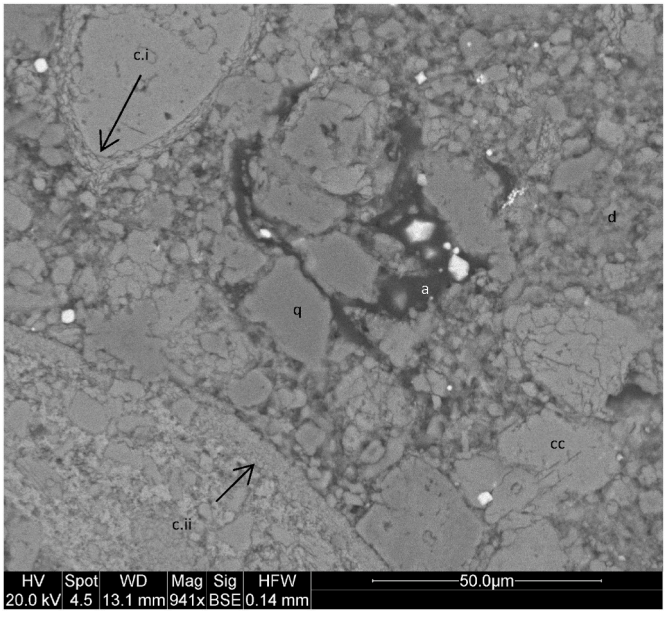

Fig. 2. A typical electron micrograph of sample U1, with mud to silt-sized quartz (q) and bioclastic calcite (c.ii) grains in an illite matrix (d) with intra and inter granular calcite cement (c.i). There is also some organic carbon (a).

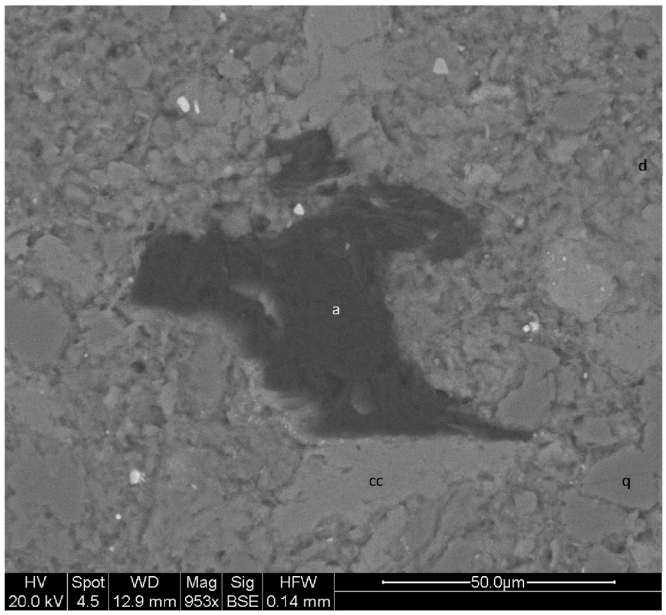

Fig. 3. An electron micrograph of a typical sample of U2, with mud to silt-sized quartz (q) and authigenic calcite (cc) grains within an illite (d) matrix with some finer-grained silicate and carbonate material (some inter-particle calcite cements). There is also some organic carbon (a).

Fig. 4. An electron micrograph of a sample of U3 with mud to silt-sized quartz (q), bioclastic and authigenic calcite (cc) grains within an illite (d) matrix with some finer-grained silicate and carbonate material. This sample is from close to the transition zone between the Utica shale and Point Pleasant Formation. There is evidence of intra-particle calcite cement (c.i) within the bioclastic calcite grains (c.ii). Within this there is some inter-particle calcite cements (c.i). There is also some organic carbon (a).

The TOC content, as expected, peaks in sample U3 from the base of the Utica Formation and is generally higher in samples (U1, U2) from the Utica Formation compared with those (U4, U5) from the Point Pleasant Formation.

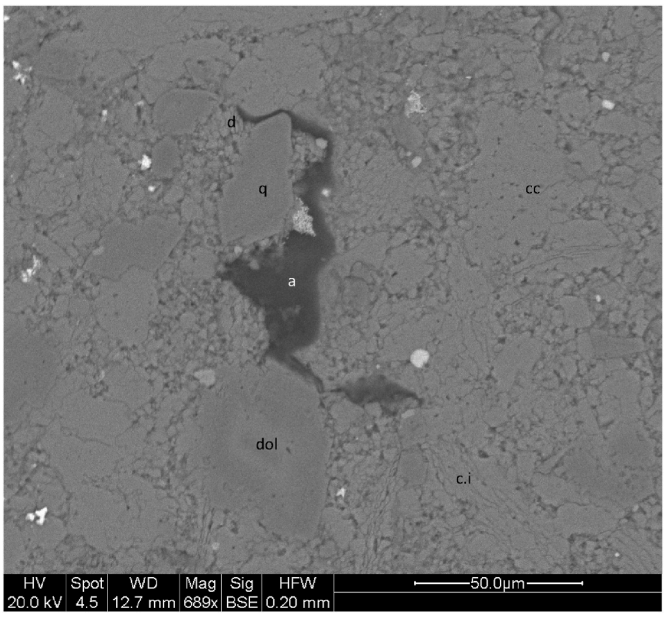

Fig. 5. An electron micrograph of a typical sample of U4, being part of the Point Pleasant Formation with coarse silt-grained carbonate zoned minerals which are comprised of calcite (cc) and dolomite (dol) due to the dolomitisation of calcite to form dolomite. There are silt-grained quartz (q) and calcite (cc) grains surrounded by an illite (d) and finer-grained carbonate matrix. Observed post-sedimentation events are some inter-particle calcite cement (c.i) and dolomitisation of the calcite. There is also some organic carbon (a).

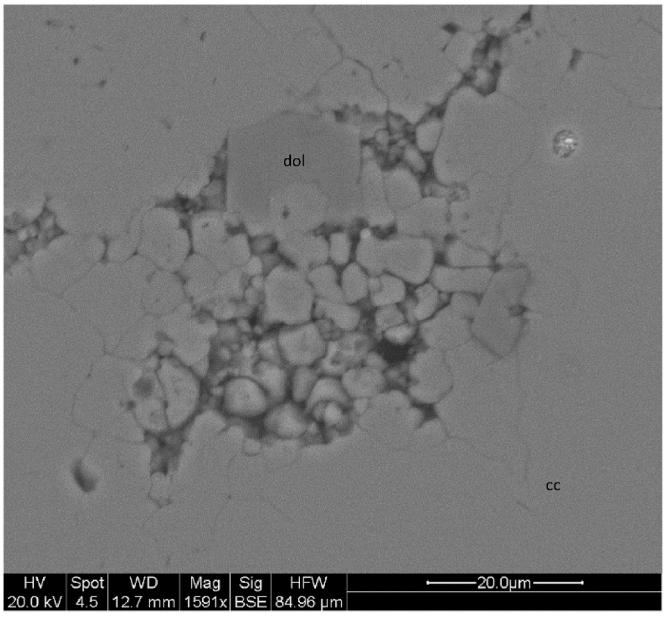

Fig. 6. An electron micrograph of a typical sample of U5, which is part of the Point Pleasant Formation with typical calcite (cc) grains (5–10 mm), there are some darker coloured minerals which have been identified as dolomite (dol).

4.2. Scanning electron microscopy

Figs. 2–6 show examples of SEM images of sections through samples of shales U1 to U5. Detailed examination of sample textures (given in Figs. 2–6) indicates that the Utica Formation samples are characterised by bioclastic carbonates with intragranular calcite cement in a fine grained illite and quartz grain matrix. Organic carbon is observed as discrete particles, running parallel to bedding, and compacted around neighbouring siliciclastic grains. However, the Point Pleasant samples are characterised by authigenic carbonates which have undergone some dolomitisation. In U5 there is some fine grained illite, but U4 is made up of a fine-grained illite matrix with coarse grained authigenic carbonate cement within it. Organic carbon is not observed in U5, but is observed in discrete particles in U4.

Table 1
Details of Utica shale samples studied in this work.

Sample name	Depth/ft
U1	5800–5803
U2	5872–5875
U3	5998–6001
U4	6102–6103
U5	6103–6106

The Utica Formation consists of dark grey to brown calcareous shale often laminated and bioturbated, with a TOC content of approximately 3.5% (Smith, 2013). Samples (U1 and U2, Figs. 2 and 3, respectively) are predominantly siliclastic siltstones with lesser amounts of bioclastic material (Table 1). The matrix is dominated by illite with lesser amounts of calcite cement. Whether the illite is primary or secondary was not determined. Organic matter is present as discrete particles or agglomerations (see Fig. 3). U3 (see Fig. 4) is taken from the base of the Utica Formation which is defined to be organic and carbonate rich (Hickman et al., 2015).

The underlying Point Pleasant Formation is overall defined by an organic-rich, calcareous shale with interbedded limestone. The Upper interval of the Point Pleasant Formation (such as samples U4 and U5 in Figs. 5 and 6, respectively), however, is an organic-poor grey shale with abundant thin limestone beds. A TOC of <1% (see Fig. 1) is typical of this interval with low organic carbon and intermediated composition in terms of the balance between siliciclastic and bioclastic material. The lower interval of the Point Pleasant Formation (below the samples studied here) is much more carbonate rich, with an average TOC content 4%–5%, is a storm-influenced formation, and has common burrows, even in the organic-rich facies (Luft, 1971; MacDowell, 1986; Hickman et al., 2015). In the locations of the borehole, from which the samples studied here were obtained, the formations were deposited on a storm dominated shelf, hypothesised to have been part of a semi-enclosed epicontinental sea (Popova, 2017).

4.3. Mercury porosimetry

Fig. 7(a) shows the raw mercury intrusion and extrusion curves for samples U1 to U5. For some samples (U1-3), the mercury intrusion curves are of a hyperbolic form at the highest pressure (corresponding to a pore size of approximately 3 nm), thereby suggesting that mercury has not been able to fill the entire void space. It is noted that, typically, very little of the mercury extruded when the pressure was reduced, and thus mercury entrapment is apparently high. The reality of the mercury entrapment, as opposed to its mere appearance due to potential sample crushing, was confirmed by CXT, and by the overcondensation data given below.

Fig. 7(b) shows the cumulative PSDs for intra-particle porosity obtained from an analysis of the raw porosimetry data in Fig. 7(a) using the Kloubek (1981) correlations.

4.4. Computerised X-ray tomography (CXT)

Fig. 8 shows typical examples of reconstructed 2D slices from the CXT imaging of the shale samples U1–U5 following the intrusion and entrapment of mercury during porosimetry, as seen in Fig. 7. Some 2D slice images of samples of fresh shale chips before mercury porosimetry are included in Appendix 3. Since mercury has a much higher electron density than the surrounding shale it absorbed many more X-rays, and

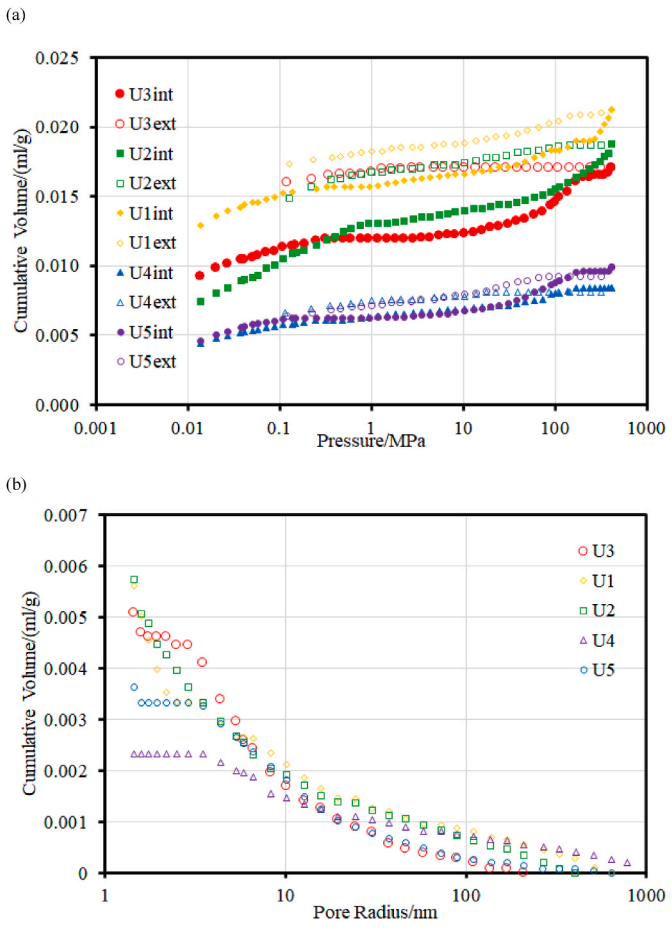

Fig. 7. (a) Raw mercury porosimetry intrusion (int) (solid symbols) and extrusion (ext) (hollow symbols) data, and (b) cumulative intra-particle pore size distributions for Utica shale samples U1 (diamonds), U2 (squares), U3 (big circles), U4 (triangles) and U5 (small circles).

appears as bright white in the images in Fig. 8, while the rock is mid-grey (and empty space is black). However, electron-dense minerals such as iron pyrites would also strongly absorb X-rays and also be expected to appear as bright white pixels. However, the CXT images of fresh samples given in Appendix 3 show that the spatial incidence of strongly X-ray absorbing minerals is very low before porosimetry. Hence, virtually all the bright white pixels in Fig. 8 are due to entrapped mercury. The presence of mercury within the sample suggests that the entrapment in the porosimetry extrusion curves is real and not just apparent, due to sample compression. The high mercury entrapment during porosimetry means that the mercury provides a good tracer for the intruded volume.

The high contrast between entrapped mercury and the rock means the images can be unambiguously gated to show only the entrapped mercury phase. Fig. 9 shows 3D reconstructions of chips of samples U1–U5 containing entrapped mercury. From Fig. 9(a), it can be seen that the pores intruded in mercury porosimetry are generally parallel to the bedding planes in the shale for sample U1, though there is some more intrusion at the edge of the sample. From Fig. 8, for sample U2, the residual mercury is predominantly entrapped in regions located in close proximity to fractures, as the mercury also picks out fainter, smaller macropores/fractures not directly visible otherwise, and the 'cloud-like' entrapped regions of mercury around them. As mentioned in Appendix 1, it is possible that some cracks may have formed during the drilling and transportation of the cores from the United States. Further cracking may have occurred when the cores were reduced to millimetre-sized chip samples for mercury porosimetry. The CXT images of fresh samples given in Appendix 3, suggest that cracking visible for these materials is limited to the edge of the chips. However, as can be seen from Fig. 8(b) the pervasiveness of cracks is low such that the order of the typical lattice size for the nanoscopic pore network will not have been affected, and thus the relative accessibility of the mesopore network will not have been greatly affected.

In contrast, from Fig. 8(c)&(d), the entrapped mercury in U3 suggests more pervasive and homogeneous mercury penetration and entrapment, but only up to a particular front in the shale. The entrapped mercury in U3 is located in broad bands and extended regions, rather than being more closely associated with fractures and adjacent borders along fractures, as for U1 and U2. This greater spatial prevalence of entrapped mercury away from defined planes or fractures also suggests greater disorder. The dark regions of the chips in the CXT images represent areas with pore necks too small to permit mercury intrusion and/or low voidage fraction. From a consideration of the grey-scale it looks most likely to be the carbonate phases that have been intruded in U3, since intrusion was in the lighter grey-scale mineral phases. The greater pervasiveness of mercury intrusion in U3, compared to U1 and U2, would then be consistent with the data in Fig. 1 which shows that U3 has much more carbonate than U1 and U2. Clays, which are more abundant in U1 and U2, are likely to have more pores too small for mercury to intrude. This is also consistent with the more pervasive distribution of entrapped mercury across the chip of U4, shown in Fig. 8(e), which, from Fig. 1, has the highest carbonate content of all samples. However, the intensity of the bright regions in Fig. 8(e) are lower than for Fig. 8(c)&(d) for U3 suggesting less mercury intrusion for U4 consistent with the lower intruded volumes for U4, compared with U3, in Fig. 7. The spatial distribution of entrapped mercury in U5, seen in Fig. 8(f), is less pervasive than for samples U3 and U4, and back to more like U2. Overall, the aforementioned findings from CXT suggest that, across the series U1–U5, also shows an evolution in the amount and spatial distribution of entrapped mercury.

4.5. Gas sorption

Fig. 10 shows the conventional nitrogen sorption isotherms, overcondensation boundary desorption isotherms, and scanning curves for the Utica shale samples. From a comparison of Fig. 10(a)–(i), it can be seen that sample U3 has the highest ultimate gas uptake in both the conventional and overcondensation experiments. U3 also has the largest amount adsorbed at the marked step at a relative pressure of approximately 0.5 in the overcondensation desorption isotherm.

The overall forms of the boundary adsorption and desorption isotherms for samples U1 to U5 in Fig. 10 are generally very similar. Following the BET region, the adsorption isotherms rise almost linearly until a relative pressure of approximately 0.6–0.7 where they begin to curve upwards, at first gently, and then more sharply beyond relative pressures of approximately 0.9. The ultimate amount adsorbed achieved for the conventional isotherms is lower than the top of the overcondensation desorption isotherm. In all cases, the overcondensation boundary desorption isotherm, broadly, consists of three regions. Following the vertical fall in amount adsorbed at relative pressure of approximately 1, that represents the evaporation of bulk condensate, the first section of the intra-particle desorption is typically a concave hyperbolic curve down until a relative pressure of approximately 0.5 where there is a steep, near vertical, step down to the lower hysteresis closure point. Thereafter the desorption isotherm overlays the adsorption isotherm, as expected for reversible multi-layer adsorption. However, sample U3 is an exception to this otherwise general pattern, since the upper part of the boundary desorption isotherm is convex, with a marked knee at a relative pressure of approximately 0.75–0.8. Further, from Fig. 10, it can be seen that the relative size of the step in the conventional desorption isotherm at a relative pressure of approximately 0.5 grows, as a fraction of the corresponding step in the overcondensation boundary desorption isotherm, for the series U1–U4. U5 has a relatively very small step at a relative pressure of approximately

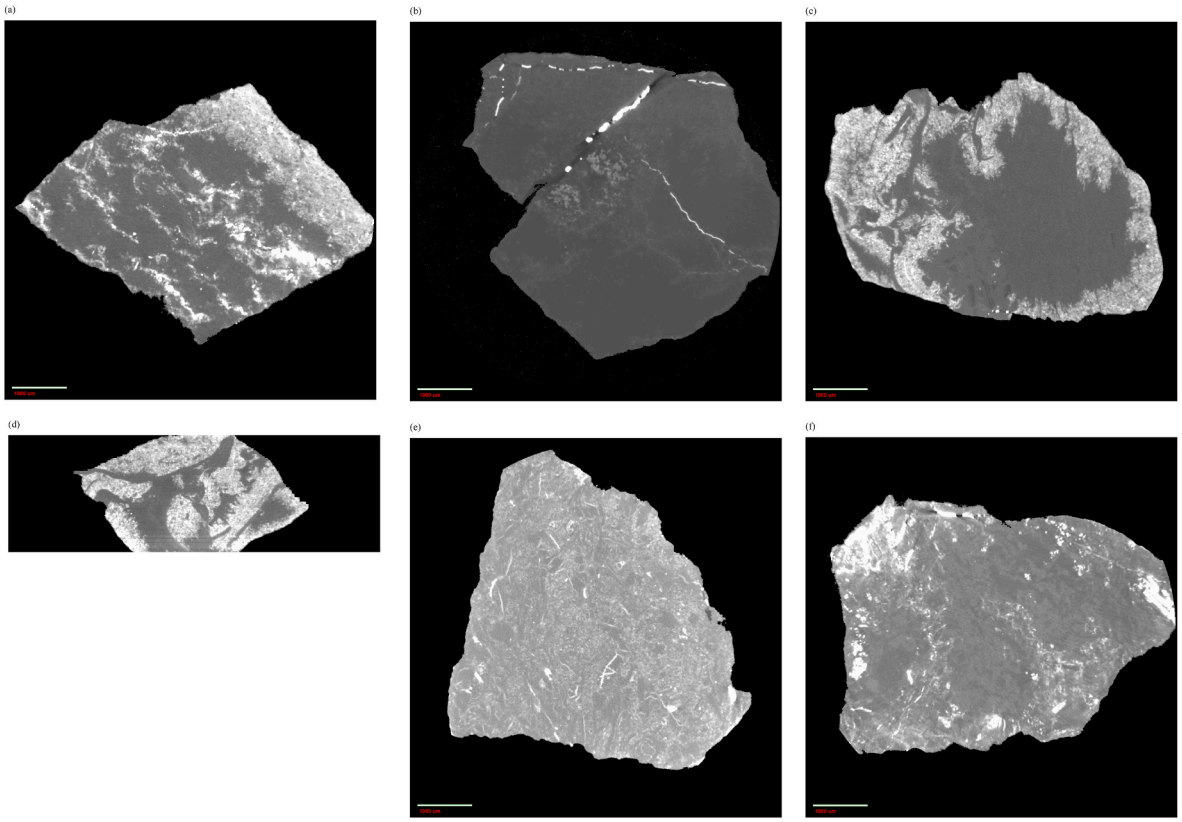

Fig. 8. Examples of 2D reconstructed slices from CXT 3D data-set for chips of (a) U1, (b) U2, (c&d (same scale)) U3, (e) U4, and (f) U5 shale following mercury porosimetry. The scale bar shown corresponds to 1000 μm.

0.5.

Given the presence of two knees in the overcondensation boundary desorption isotherm for U3, it was decided to probe the hysteresis for all samples with ascending scanning loops springing from the relative pressures in the regions of the U3 isotherm where the knees occur. Hence, in all cases, the ascending branches of two scanning loops were initiated at relative pressures of 0.5 (henceforth denoted scanning loop 1, SL1) and 0.8 (SL2), respectively, on the overcondensation boundary desorption isotherm, and the descending branches of both loops were initiated at a relative pressure of 0.995. The corresponding pore radii for these relative pressures from the Broekhoff and de Boer (BdB) (1967,1968) method for hemispherical menisci are 2.6 (SL1), 6.4 (SL2), and approximately 300 nm, respectively. From Fig. 10, it can be seen that, for all samples, both the scanning loops have an overall crescent shape. The ascending branches of the scanning loops cross the majority of the hysteresis gap with very little additional adsorption, and then rise sharply as they approach the region of the boundary adsorption isotherm. Desorption commences immediately on the descending branch of the loops and, in some cases, U2 and U3 particularly, hysteresis remains relatively narrow compared to the width of the hysteresis between the boundary curves. However, the relative juxtaposition of the loops changes between samples. While, for samples U1 and U5, the ultimate amount adsorbed at the top of the adsorption branch increases markedly over the series consisting of the conventional isotherm, SL1, and SL2, the corresponding amounts adsorbed are very similar for sample U4. Samples U2 and U3 show behaviour intermediate between the two. It is also noted, that for sample U1, the conventional desorption isotherm, SL1 and SL2 do not cross each other. Although, it is the case that the ascending branch of SL1 overlays the conventional desorption isotherm for relative pressures approximately 0.91–0.97, while the descending branch overlays the ascending branch of SL2 over the relative pressure range approximately 0.95–0.98. In contrast, for sample U2, the ascending branch of SL2 unambiguously crossed the position of the descending branch of SL1. Further, for samples U3 and U5, the ascending branch of SL1 crossed the conventional desorption isotherm. For sample U4, the ascending branches of both SL1 and SL2 cross the conventional desorption isotherm. In addition, it is noted that the descending branches of both SL1 and SL2 for sample U4 more or less overlay the overcondensation boundary desorption isotherm, whereas for samples U1 and U5 it is only the desorption branch of SL2 that overlays the boundary desorption isotherm. This suggests that the ranges of pore body and neck sizes involved in the scanning loops are different in each sample. The aforementioned forms of the scanning loops will be interpreted further in the Discussion.

Fig. 11 shows the variation across the shale series U1-5 of the organic matter mass fraction from the fits to the aforementioned homotattic patch models with either fractal BET or finite multilayer BET equations. Also shown in Fig. 11 is the variation across the Utica shale series U1-5 of the total organic carbon. From Fig. 11, it can be seen that the TOC and the organic matter isotherm contribution fractions all show a rising and falling trend with a peak for sample U3. This shows how the parameter optimisation for the homotattic patch model fitting procedure is able to distinguish samples which have the greatest contribution from their organic content component.

Despite the variation in the absolute values of the organic matter fractions for the respective fits to the homotattic patch models involving fractal BET or finite multilayer BET equations, both produce the same distribution of values which allow for consistent comparisons across a dataset for either model to assess the impact that the organic component of the sample has. It is also noted that the TOC data includes a contribution from that which is inaccessible to the exterior. However, overall, the isotherm homotattic model fitting suggested that the higher accessible surface area present in U3 shale is organic material, due to the higher TOC.

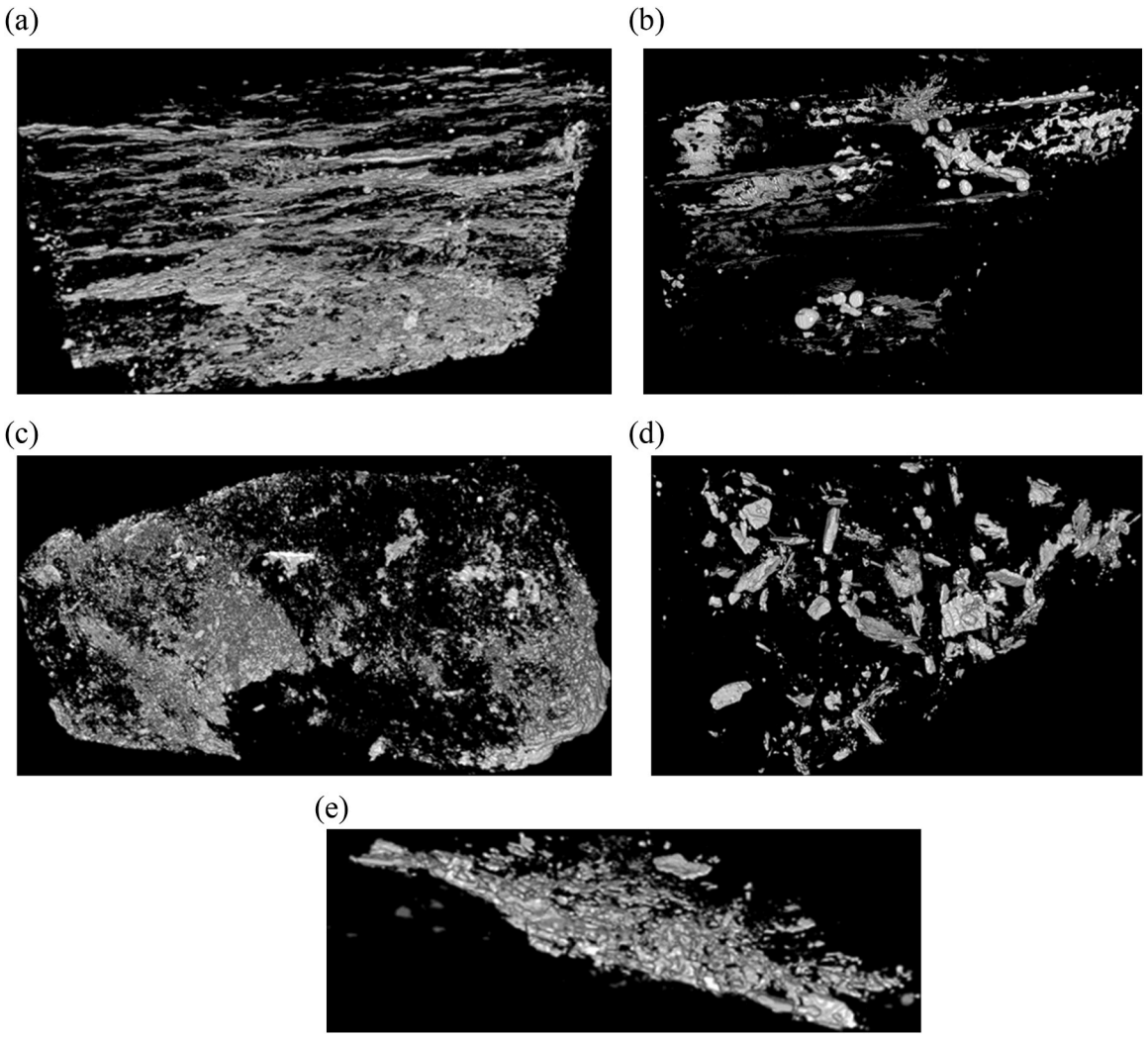

Fig. 9. Examples of 3D reconstructions of the locations of entrapped mercury obtained from CXT images of chips of (a) U1, (b) U2, (c) U3 (d) U4, and (e) U5 shale following mercury porosimetry.

Fig. 12 compares the conventional sorption isotherms and overcondensation desorption isotherm for samples of shale U3 in chip (approximately mm particle size) and powder form. It can be seen that the ultimate amount adsorbed increased for the powder sample in both conventional and overcondensation experiments. It is also noted that the sharpness of the higher knee in the overcondensation boundary desorption isotherm is slightly reduced for the powder sample. It can also be seen that neither of the conventional desorption isotherms for chip or powder samples have any sign of convexity.

The complete neck PSD, including macropores, can be obtained from the overcondensation boundary desorption isotherm, such as via the Barrett-Joyner-Halenda (BJH) method (Gregg and Sing, 1982). This PSD can be compared with that obtained from mercury intrusion (given in Fig. 7(b)). For example, for the sample U3 with the largest mercury intrusion of intra-particle porosity, it has been found (see Fig. 13) these two techniques give rise to near-identical shapes for the PSDs, over an overlapping size range, even for different samples of same material, thereby suggesting that the mercury pressure is not simply crushing the sample. This suggestion is also supported by the presence of the actually intruded, and then entrapped, mercury observed in the CXT data in Fig. 8(c and d).

5. Discussion

5.1. Model for the typical pore structure of the shales

A transition across the series U1-5 is evident in the pore structure as manifested in the gas sorption data. The crossing ascending scanning curves obtained here for Utica shales are similar in type to those obtained for Rempstone shale by Rigby et al. (2020) and for Middle Eastern shales by Barsotti et al.(2020), probably because the underlying pore geometries of Utica and Rempstone shales probed by scanning data have some similarities. The overall form of the conventional adsorption isotherm, overcondensation boundary desorption isotherm, and scanning loops suggests a void space consisting of large pore bodies shielded by narrow pore windows with a relatively much wider range of sizes than for the bodies, as shown in Fig. 14(a). The pores thus have a typical shape similar to a jam-jar (preserve jar). The relatively flat (almost horizontal for U5) form of the conventional adsorption isotherm, and the ascending branches of SL1 and SL2, for relative pressures in the range approximately 0.50–0.85 (corresponding to pore sizes of approximately 4–12 nm), followed by a steep rise at high relative pressures, suggests capillary condensation in pore bodies of just relatively larger sizes, as seen in Fig. 15. In contrast, the overcondensation boundary desorption isotherms show steady declines in amount adsorbed over the whole relative pressure range from 0.995 to 0.5 (corresponding to pore sizes of

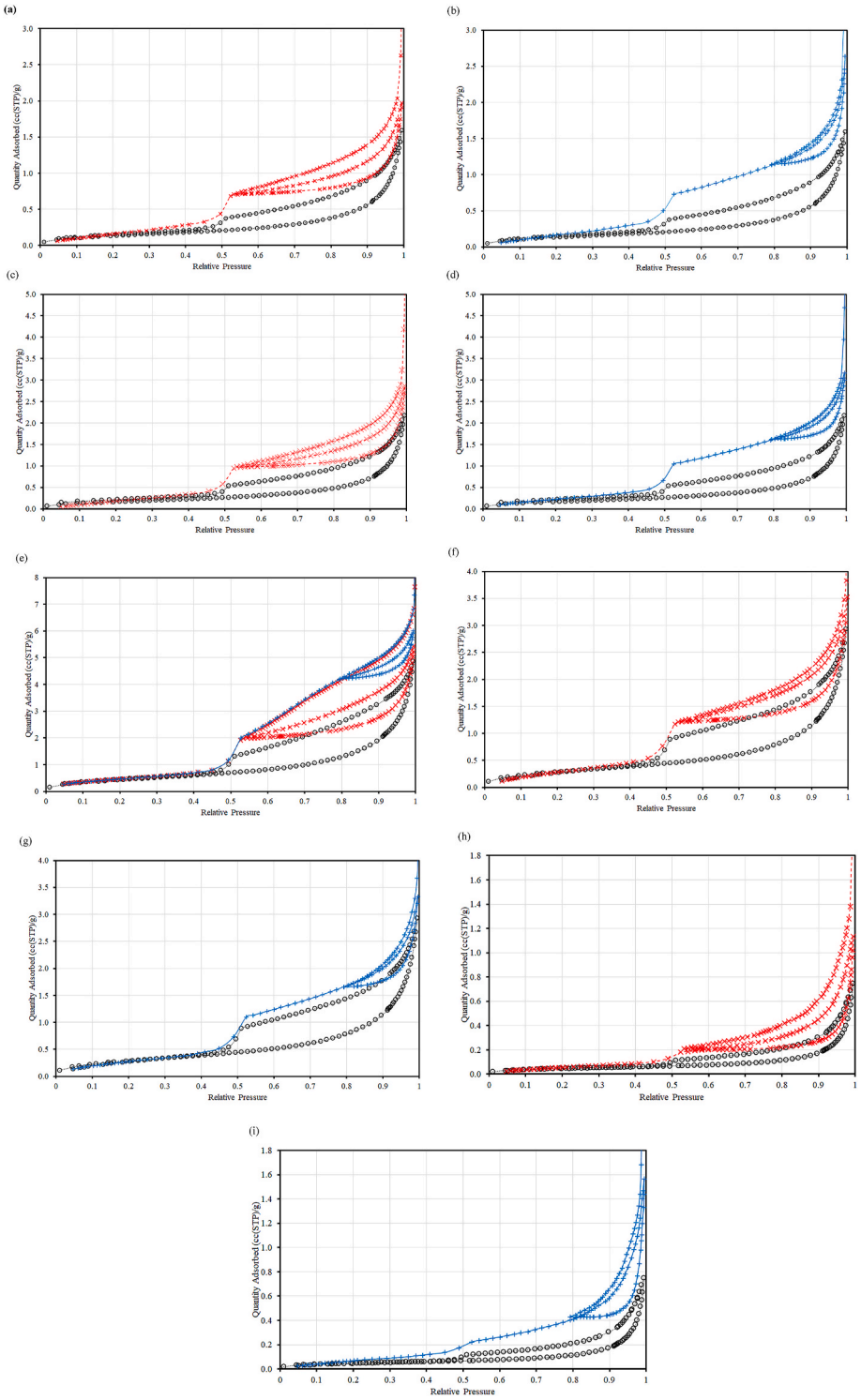

Fig. 10. Conventional nitrogen sorption isotherms (○), overcondensation boundary desorption isotherms (× ,+), and two scanning loops (SL1, × ; SL2, +) for chip samples of Utica shales U1 (a,b), U2 (c,d), U3 (e), U4 (f,g) and U5 (h,i).

approximately 500–5 nm), apart from the hiatus for sample U3 at a relative pressure of approximately 0.75–0.8. This suggests a much wider range of shielding pore window sizes than pore body sizes, which means pore bodies steadily empty in order of shielding necks down the overcondensation isotherm as seen in Fig. 15.

The very wide range of relative pressures over which amount adsorbed declines on the boundary desorption isotherm suggests that even larger windows have direct external access and the corresponding model for the pore structure would be like an array of similar jam-jar-like pores with a range of mouth sizes, as seen in Fig. 14. These pore mouths may also empty directly into the type of large macropores evident in the CXT images of samples U1 and U2 after mercury entrapment in Fig. 8, as these would empty at the very top of the desorption isotherm. The 'penumbra' of entrapped mercury bordering the mercury-filled macroporosity in the CXT images of U2 may represent entrapment within this jam-jar porosity along their length.

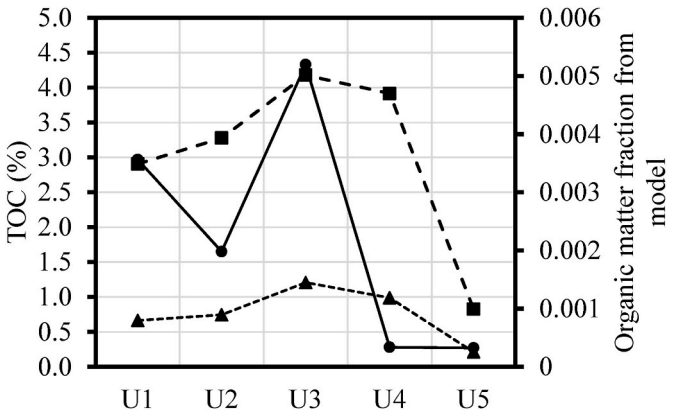

Fig. 11. Variation across the shale series U1-5 of the organic matter mass fraction from the fits to the homotattic patch models with either fractal BET (eq. (6)) (triangles) or finite multilayer BET (eq. (7)) (squares). Also shown is the variation across the Utica shale series U1-5 of the total organic carbon (TOC, circles).

5.2. *Pore-to-pore co-operative effects in gas sorption data*

However, there is also evidence for pore-to-pore co-operative effects in sorption, and, thus, also more network complexity. The aforementioned hiatus in the overcondensation boundary desorption isotherm at relative pressures approximately 0.75–0.8 (corresponding to pore sizes of approximately 10–17 nm) for sample U3 is a percolation knee. The pause in the decline in amount adsorbed is caused by shielding of pore body and neck sizes larger than the knee by the smaller neck sizes at the knee, as shown schematically in Fig. 16. This enhanced shielding arises when the spatial juxtaposition of pore necks (and bodies) is more jumbled. The presence of greater shielding is also consistent with the reduction in the sharpness of the percolation knee with the decline in particle size from chip to powder evident in Fig. 12, since a reduction in lattice size of a random pore network leads to a smearing out of the percolation transition due to less shielding arising in smaller lattices (Seaton, 1991). According to critical path theory, the development of a percolation knee corresponds to the emergence of a critical single pore size that controls mass transport across the larger network (Ambegaokar et al., 1971; Katz and Thompson, 1986). Identification of this critical pore size is a form of upscaling more similar to attempted with multi-scale imaging, whereby characteristic properties at a lower length-scale represent features over a larger length-scale.

It is noted that the sign of greater complexity in the desorption data (the percolation knee) occurs for the same sample, U3, for which the mineralogy data in Fig. 1 also suggests has a more complex mixture of components, and the SEM data (Figs. 2–6) suggests has a more jumbled spatial arrangement of component mineral grains and inter-granular cements. The overall crossover from high illite content to high calcite content, and spike in TOC, around the depth of sample U3, together with the morphological data indicating increased disorder in this sample, suggests that some sort of high energy transition from a primarily marine to a primarily terrestrial source of sediments occurred, that also caused a transient increase in influx and/or lay-down of organic material in the sediments. The existence of this evidence for the high disorder in the complex sediments in U3 suggests it was rapidly fixed by relatively swift subsequent burial and inter-granular cementation processes following initial lay-down, since otherwise it would have been removed by longer timescale processes.

Besides the pore-to-pore co-operative effect (pore-blocking) in the desorption data there is also evidence for network-related co-operative effects in the adsorption data too. The ultimate amount adsorbed at the top (highest pressure) of the conventional adsorption isotherm (CAI) and the ascending branches of SL1 and SL2 increases in that order for samples U1 and U5. Further, the ultimate amount adsorbed for SL1 and SL2 for sample U2 is much higher than the ultimate amount adsorbed on the conventional adsorption isotherm. The difference in step heights, at relative pressure of approximately 0.5 (corresponding to a pore size approximately 4–5 nm), between the conventional and overcondensation desorption isotherms suggests that some of the very largest pores filled only by overcondensation remain filled with condensate even down to a relative pressure of approximately 0.5, as shown in Fig. 15. This is because (as shown schematically in Fig. 14(a)) the very largest pores (pore J, in Fig. 14(a)) are shielded by very narrow pore necks of sizes (diameters) smaller than approximately 4 nm (necks H & I in Fig. 14(a)), and the aforementioned step in desorption is due to the cavitation effect (Gregg and Sing, 1982). For SL1, these very largest pores, shielded by very narrow necks, remain filled at the start of the loop, in addition to those that would be filled by the conventional

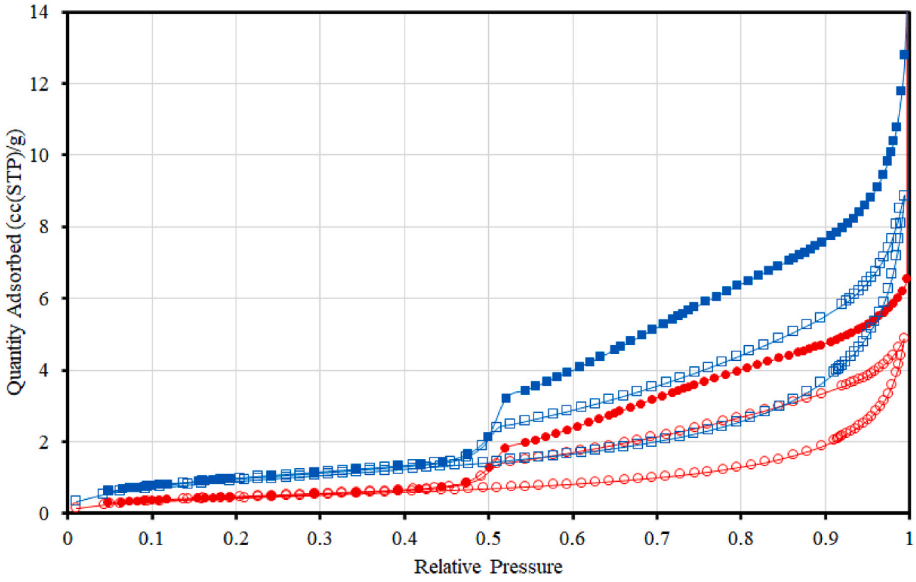

Fig. 12. Conventional nitrogen sorption isotherms (open symbols) and overcondensation boundary desorption isotherms (solid symbols) for chip (red circles) and powder (blue squares) form samples of Utica shale U3. (For interpretation of the references to colour in this figure legend, the reader is referred to the Web version of this article.)

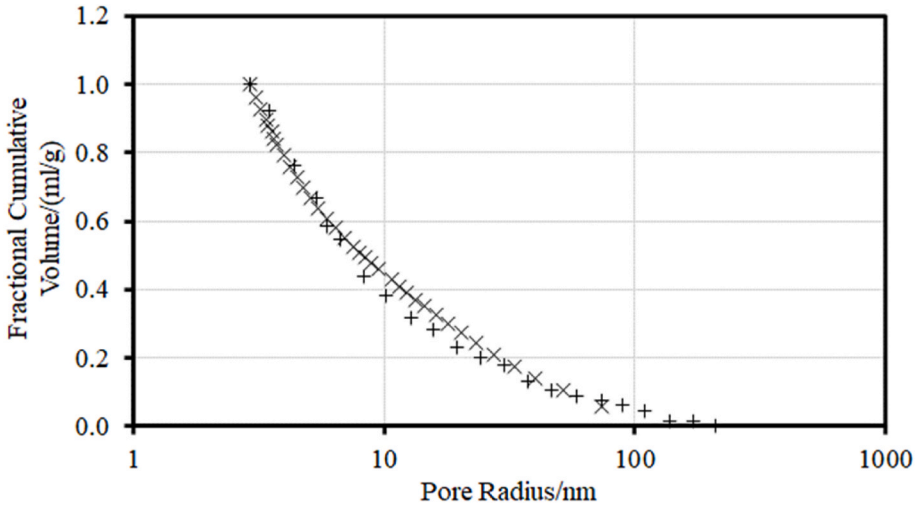

Fig. 13. Comparison of cumulative pore size distribution from gas overcondensation (BJH method with Harkins-Jura *t*-layer (Rigby, 2020)) (×) and mercury intrusion (and Kloubek (1981) correlations) (+) for samples of U3.

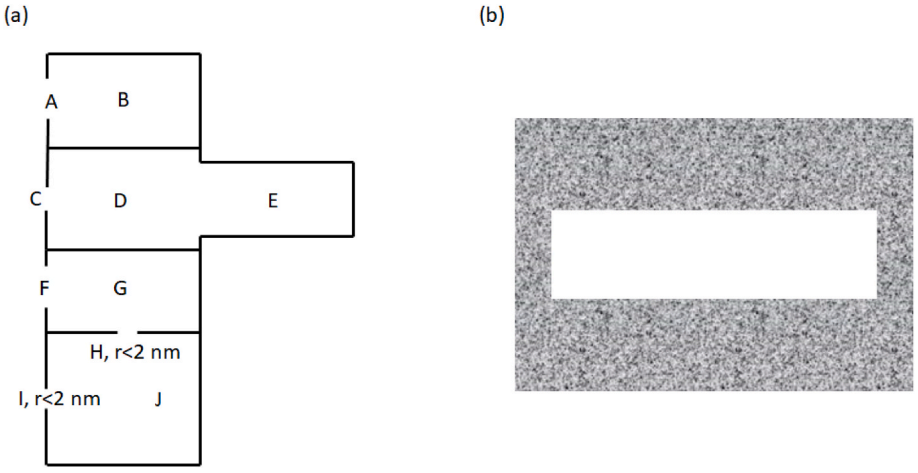

Fig. 14. Schematic depictions of the model pore spatial arrangements probed by scanning loops in samples (a) U1, U2 & U5, and (b) U3 described in the main text. The model in part (a) is the 'jam-jar' type arrangement with inter-connections, with the bottom very largest pore shielded by very narrow necks. The model in part (b) has a large macropore surrounded by a disordered 'sea' of smaller pores.

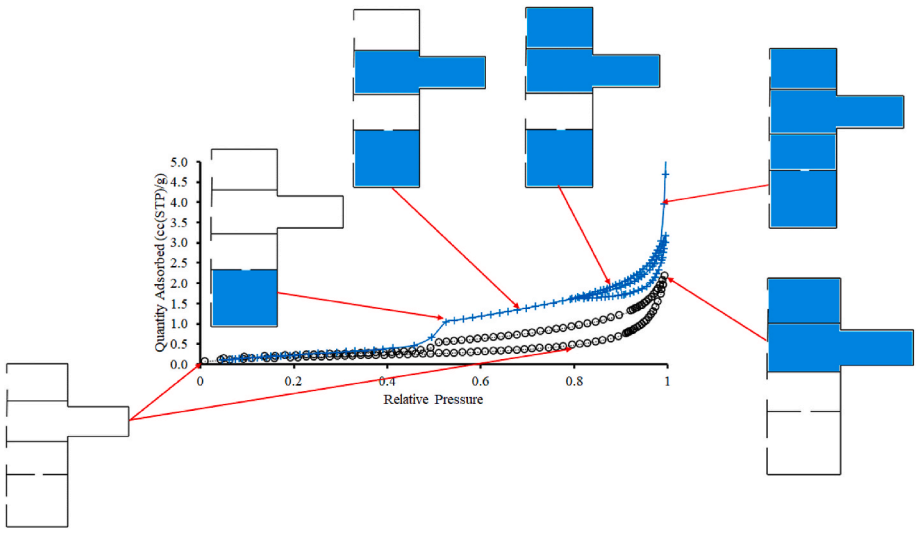

Fig. 15. Schematic diagram showing the state of pore-filling with condensate (blue shading) of the model pore system shown in Fig. 14(a) at various positions (indicated by red arrows) around the conventional and overcondensation isotherms of the form found in this work. Regions left white represent vapour-filled pores. It is noted that the multilayer film build-up is omitted for simplicity. (For interpretation of the references to colour in this figure legend, the reader is referred to the Web version of this article.)

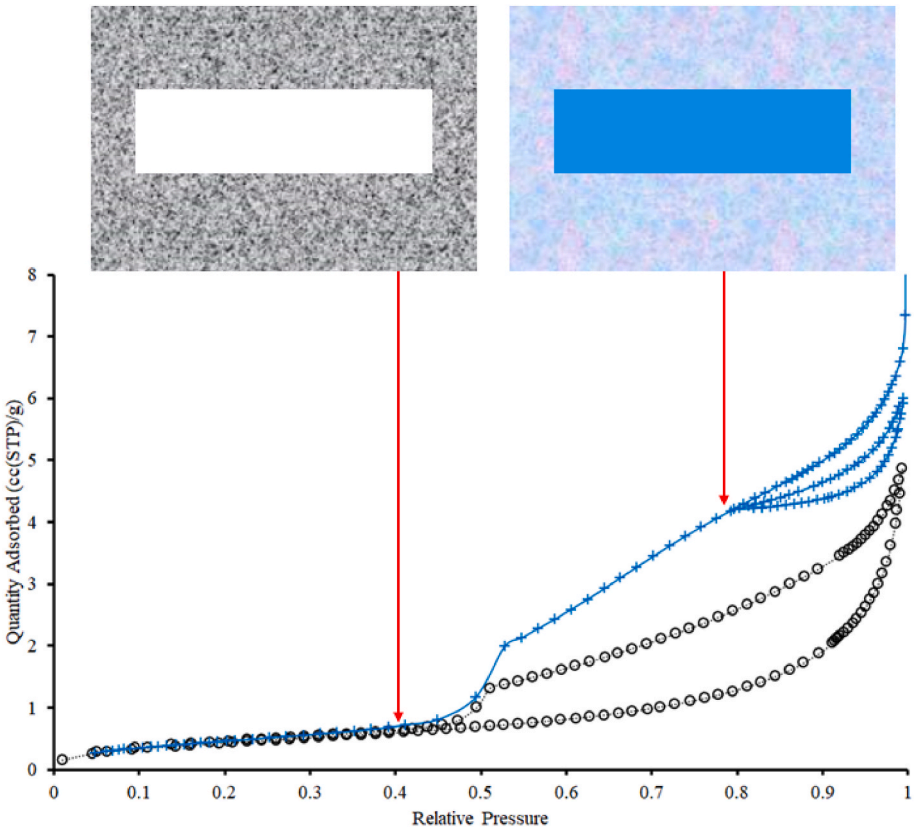

Fig. 16. Schematic diagram showing the state of pore-filling with condensate at two positions along the overcondensation desorption isotherm for the pore structural model, given in Fig. 14(b), for shale sample U3. The blue shading represents pores filled with condensate, while white represents an empty pore. (For interpretation of the references to colour in this figure legend, the reader is referred to the Web version of this article.)

adsorption isotherm. Hence, this head-start in condensate amount means that the ultimate adsorption volume for SL1 will necessarily be higher than that for the conventional isotherm. However, it is noted that, for SL1, for samples U1, U2 and particularly U5, the additional ultimate amount adsorbed, compared to the conventional isotherm, is actually larger than that anticipated simply from the difference in step height, at relative pressure of approximately 0.5, between the overcondensation and conventional desorption isotherms. This means some additional adsorption is occurring on the ascending branch of SL1, for samples U1, U2 and U5, than occurred on the corresponding conventional adsorption isotherm. This is because the presence of residual condensate in some larger pore bodies (pore J in Fig. 14(a)) may mean that adjoining empty pore bodies connected via narrower windows (like pore G in Fig. 14(a)) may, themselves, fill with condensate at a lower relative pressure, via a hemispherical meniscus rather than via a cylindrical-sleeve meniscus in a co-operative adsorption effect (Rigby, 2018, 2020). This is shown schematically in Fig. 17. This means that the ultimate pressure at the top of the scanning loop adsorption branches exceeds the filling pressure of more pores than is the case for the conventional adsorption isotherm starting with no already filled pores. Hence, the pores that fill via hemispherical menisci at the pressures towards the upper end of SL1 for samples U1, U2 and U5 are specifically the large pores that adjoin, and inter-connect with, the very largest pores blocked by narrow necks of sizes below approximately 4 nm (see Figs. 14 (a) and 17). While pore-blocking can only arise from pores located between a given pore and the path(s) to the exterior, co-operative condensation can arise from neighbouring pores in any direction, including laterally (as in Fig. 17), or towards the interior. This feature of the two effects allows them to be utilised independently in interpreting gas sorption data. The presence of co-operative condensation thereby

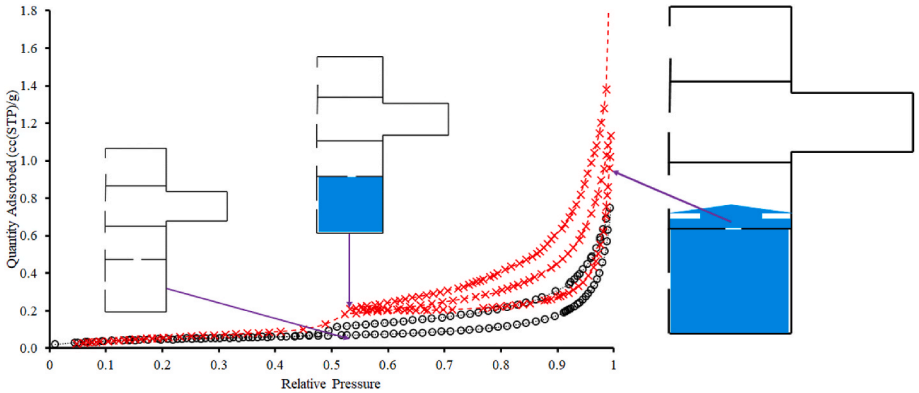

Fig. 17. Schematic diagram showing pore filling via a co-operative pore-to-pore mechanism, as described in main text. The blue shading indicates the presence of condensate and the arrow indicates the direction of the co-operative pore-filling process originating from the still-filled pore body. The diagram also shows the difference in pore-filling at the springing off point for SL1, compared with the boundary adsorption isotherm at the same pressure. (For interpretation of the references to colour in this figure legend, the reader is referred to the Web version of this article.)

suggests that rather than being largely disconnected jam jar pores, the pore bodies do form an inter-connected network via adjoining necks.

For sample U5 the ultimate amount adsorbed for SL2 exceeds that for SL1, and the desorption branch for SL2 follows, more or less, the overcondensation boundary desorption isotherm, suggesting there are no even larger pores left unfilled at the top of SL2. The additional ultimate amount adsorbed for SL2, over and above its initial head-start on SL1 (the vertical distance between the springing off point for SL2 and the adsorption branch of SL1 at the same pressure), must result from co-operative adsorption initiated from pores still left filled at the springing off point of SL2, but unfilled at the inception of SL1 and the conventional adsorption isotherm. The SL2 head-start pores thus must be shielded by pore necks that empty on the boundary desorption isotherm below the springing-off point of SL2 but before the step at relative pressure of approximately 0.5. Hence, the spatial juxtaposition of the particular pores surrounding those that fill additionally for SL2 in U5 can be deduced from the overcondensation and SC data.

The similarity in ultimate adsorbed amounts for SL1 and SL2, and also their closeness to the ultimate amount adsorbed for the conventional isotherm too, found for sample U4, as compared to U1, suggests that there are fewer very large pore bodies in the distribution for U4 than that for U1. This is consistent with the much lower intra-particle intruded volume in the mercury porosimetry data for U4 compared to U1 and U3. In addition, this suggestion is also reflected in the fact that the step at a relative pressure of approximately 0.5 in the conventional desorption isotherm is a larger fraction of the height of the corresponding step in the overcondensation desorption isotherm, meaning relatively more pore bodies shielded by very narrow pore necks (<approximately 4 nm) are filled in the conventional experiment.

5.3. Width of hysteresis in gas sorption data

The width of the hysteresis between the adsorption and desorption branches of the scanning loops varies amongst the various examples in the data in Fig. 10. However, there are key trends in this variation. It is noted that the thinnest hysteresis occurs for those cases when the ultimate amount adsorbed for that loop, compared to those of the other loop or the conventional adsorption isotherm, suggests that many more of the largest pore bodies are left unfilled with condensate (ie there is a big gap between the top of the loop and the overcondensation isotherm). Conversely, the widest hysteresis (when desorption is nearest the path of the boundary desorption isotherm), such as that for both loops for sample U4, occurs when there is relatively less difference between the complete pore filling at the top of the overcondensation boundary curve and the top of the loop itself. When large pore bodies (say like pore K in Fig. 18) are left unfilled at the top of adsorption branches they provide alternative locations, in addition to the exterior of the sample, into which condensate (such as in neighbouring pore L in Fig. 18) can evaporate via free menisci, thereby making desorption easier (ie earlier), in the sense that pore-blocking is reduced. This process is known as seeded percolation (Parlar and Yortsos, 1988). In Fig. 18, pore K acts as the seed site for the penetration of the vapour phase into pore L. For this to happen in the shale there must be connections or windows between the largest pore bodies left unfilled with condensate, and the pores that fill on the adsorption branches of the loops or boundary adsorption isotherm.

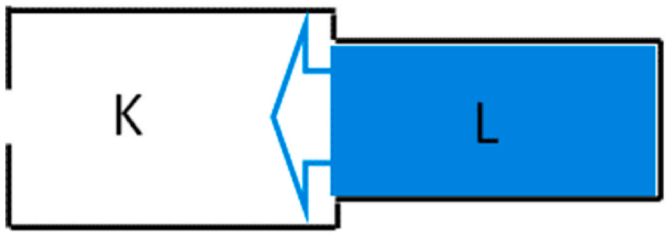

Fig. 18. Schematic diagram of the seeded percolation process. The blue shading represents the presence of liquid condensate, while regions left white represent vapour-filled pores. The arrow signifies the presence of a free meniscus from which desorption can occur in the direction shown. (For interpretation of the references to colour in this figure legend, the reader is referred to the Web version of this article.)

It is noted that, for the series of SL2s for samples from U1 to U3, the ultimate adsorbed amount at the top of the loop (ie the loop height) decreased relative to the corresponding adsorbed amount on the overcondensation isotherm, and the hysteresis width of the loop decreased from the maximum possible. Therefore, the gap between the top of the SL2 and the overcondensation isotherm, and the gap between the desorption branch and the boundary desorption, increased, across the series. However, for the next sample in the series, U4, the height and width of the SL2 had returned to the maximum possible, as for sample U1. It is also noted that the amount (shown by intra-particle intruded volume) of the largest, accessible pores, detected by mercury intrusion porosimetry, also increases in the series U1 to U3 and then drops back down markedly for sample U4. This correlation between the trends in gas sorption SLs and mercury porosimetry data suggests the trend in the SL2s occurs because of the increasing prevalence of very large pore bodies that can act as percolation seeds (as suggested by greater spatial dispersion of entrapped mercury in CXT images of U3), which then disappear again for U4 (where CXT pixel intensity is reduced relative to U3). Hence, the width of the hysteresis of the scanning loops indicates when there is a close juxtaposition and good interconnections between the pore sizes that fill in the loop and the very largest pores in the material. The very largest pores in U3 must be shielded by smaller pores that have critical pressures such that they empty on the overcondensation boundary desorption isotherm towards the springing off point of SL2, since, otherwise, this boundary curve would have taken a path more similar to that of the desorption branch of SL2.

Experiments in glass micro-models by Wardlaw and McKellar (1981) have shown that the shielding of larger pore bodies by narrow necks, or a surrounding sea of smaller pores, leads to high mercury entrapment. Hence, the proposed juxtaposition of pore sizes above for U3 is consistent with the high mercury entrapment observed in the porosimetry data for sample U3. The more pervasive and jumbled locations of entrapped mercury, observed in the CXT images of sample U3 after porosimetry, suggest a more disordered structure than U1 and U2. Fig. 14 shows schematic diagrams of the pore size spatial arrangements for samples before (U1) and at (U3) the palaeodepositional transition.

The thinning of the hysteresis of SL2 tracks the development and loss of the largest pores, and the thinnest hysteresis corresponds to the crux of the paleodepositional transition occurring at the depth of sample U3. However, the development of the percolation knee on the overcondensation boundary desorption isotherm for U3 below SL2 means that, at this transition, the next set of pores down are surrounded by a more complex network structure containing the smaller pore (-neck)s (of sizes approximately 10–17 nm) that provide the pore shielding that the knee represents (see Fig. 14(b)).

6. Conclusions

The mineralogical, SEM and multilayer adsorption data have revealed the presence of a paleodepositional transition in the Utica shale series U1-5, associated with a change-over in the predominant inorganic phase and a peak in the organic phase. The overcondensation desorption isotherm data has demonstrated the presence of very large pore bodies not detected in conventional sorption experiments, and the scanning curves have revealed their structural relationship to smaller pores below the limits of many imaging modalities. Hence, overcondensation allows the bridging between very diverse length-scales in the pore structure. Further, uniquely in the depth series considered, the overcondensation desorption isotherm for sample U3 exhibits a percolation knee, consistent with the presence of a more complex, disordered pore structure at

this depth, not evident in the conventional sorption data. The disorder in the pore structure, represented by the percolation knee, is consistent with the more complex mixture of mineralogical phases present in U3. Complementary integrated mercury porosimetry and CXT data has also shown an evolution in the macroscopic spatial distribution of the accessible nanoporosity across the depositional transition. This is associated with the changes in amount and spatial disposition of the carbonate minerals.

Declaration of competing interest

The authors declare that they have no known competing financial interests or personal relationships that could have appeared to influence the work reported in this paper.

Acknowledgements

This work was supported by the Natural Environment Research Council [grant number NE/M00578X/1]. SPR, DJL, and EP also thank the University of Nottingham for the award of a partial PhD studentship. The authors thank Martin Corfield and Elisabeth Steer (of the Nottingham nmRC) for assistance with acquiring the CXT and SEM data, respectively. We would also like to thank Schlumberger for the kind donation of a kerogen sample, and Virginia Tech for the donation of the Utica core samples.

Appendix 1

Core Description

U1

Clay sized grain shale with planar lamination and no evidence of bioturbation at core scale. Cracks in the core are presumed to be as a result of drilling from depth, and transportation from the United States.

U2

Clay sized grain shale with predominantly planar lamination, there is some potential evidence of additional mineralogical input between laminations although we cannot be confident that this has not been imbibed during the drilling process.

U3

Clay sized grain shale with a mix of planar and wavey laminations. There are visible pore network openings on the surface of the core and a mineralogical transition at 5.5 cm (on the ruler) from a darker to lighter mineral phase. Cracks in the core are presumed to be as a result of drilling from depth, and transportation from the United States.

U4

This sample has clay sized grains which are in three phases from 2 to 3 cm, 5–6 cm and 10–11 cm. These sections have wavey laminations and there is some additional mineral input in 5–6 cm and 10–11 cm from the underlying parts. From 3 to 5 cm and 6–10 cm there is a coarser grained section with some pore openings to the core surface, as well as some vein like mineral phases in wavey laminated layers.

U5

Very fine grained sample with no visible laminations, there's some isolated areas of darker sediment, juxtaposed by some more vein like mineral phase. From 3 to 6 cm vertically, half-way across horizontally there is a separation in the lighter grey sediment with a column of darker sediment due to a mud injectite where it's been overpressured and flamed through the overlying section. The areas of lighter colour which are more round in nature are only on the surface and believed to be an artefact of the drilling process.

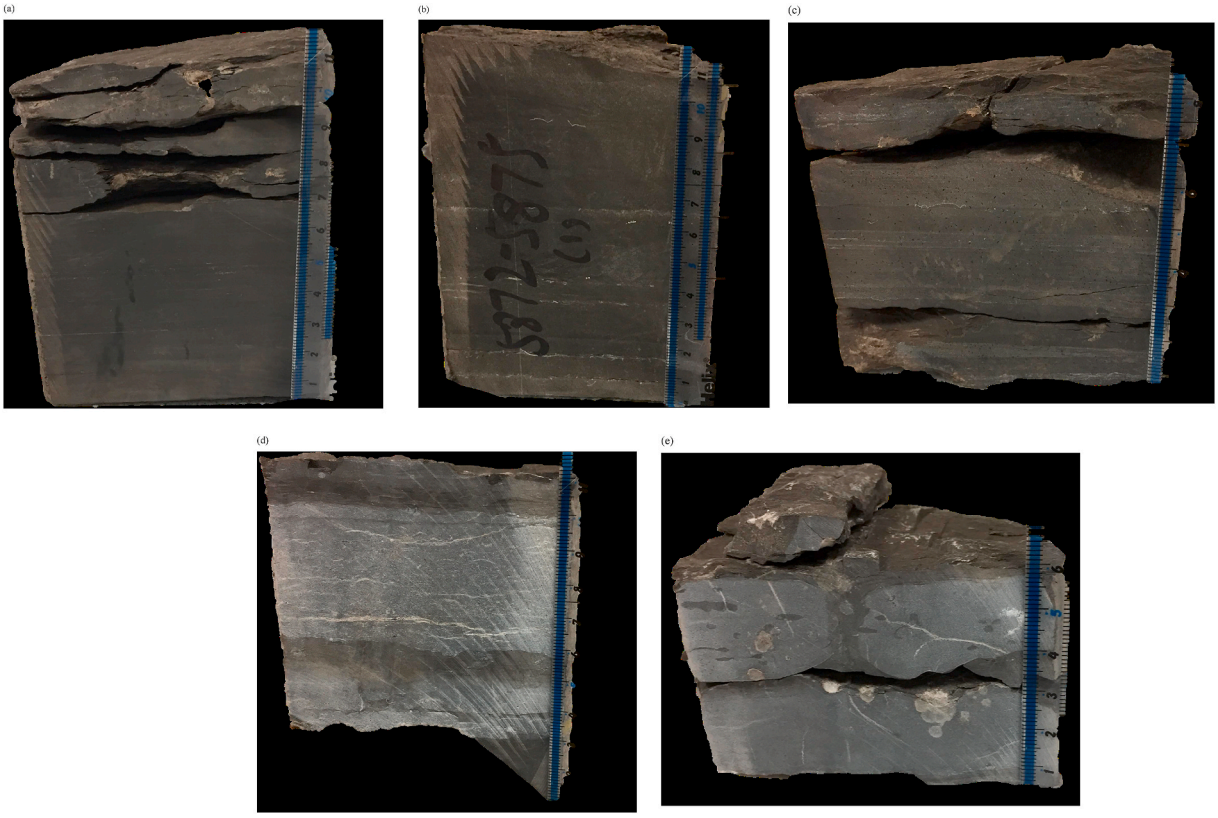

Fig. A1.1. Photographs of the core samples (a) U1, (b) U2, (c) U3, (d) U4, and (e) U5.

Appendix 2

Table A2.1
Full mineral composition for shale samples from SEM-MLA

Comp./%	U1	U2	U3	U4	U5
Calcite	21.45	14.095	52.255	69.64	60.49
Dolomite	3.45	1.47	3.61	9.92	1.86
Illite	49.94	58.885	25.365	10.015	0.565
Kaolinite	0.06	0.04	0.01	0	0
Geothite	0	0	0	0	0
Quartz	9.11	6.9	12.8	4.615	32.885
Muscovite	8.825	11.345	0.56	0.755	0.025
Albite	1.18	1.14	0.6	0.04	0
Pyrite	0.24	0.39	0.38	0.08	0.01
Chalcopyrite	0.57	0.83	0.46	0.31	0
Sphalerite	0	0	0	0	0.01
Apatite	0.285	0.175	0.59	1.415	0.195
Rutile	0.7	0.07	0.02	0	0
Unknowns	4.19	4.66	3.35	3.21	3.96
Total	100	100	100	100	100

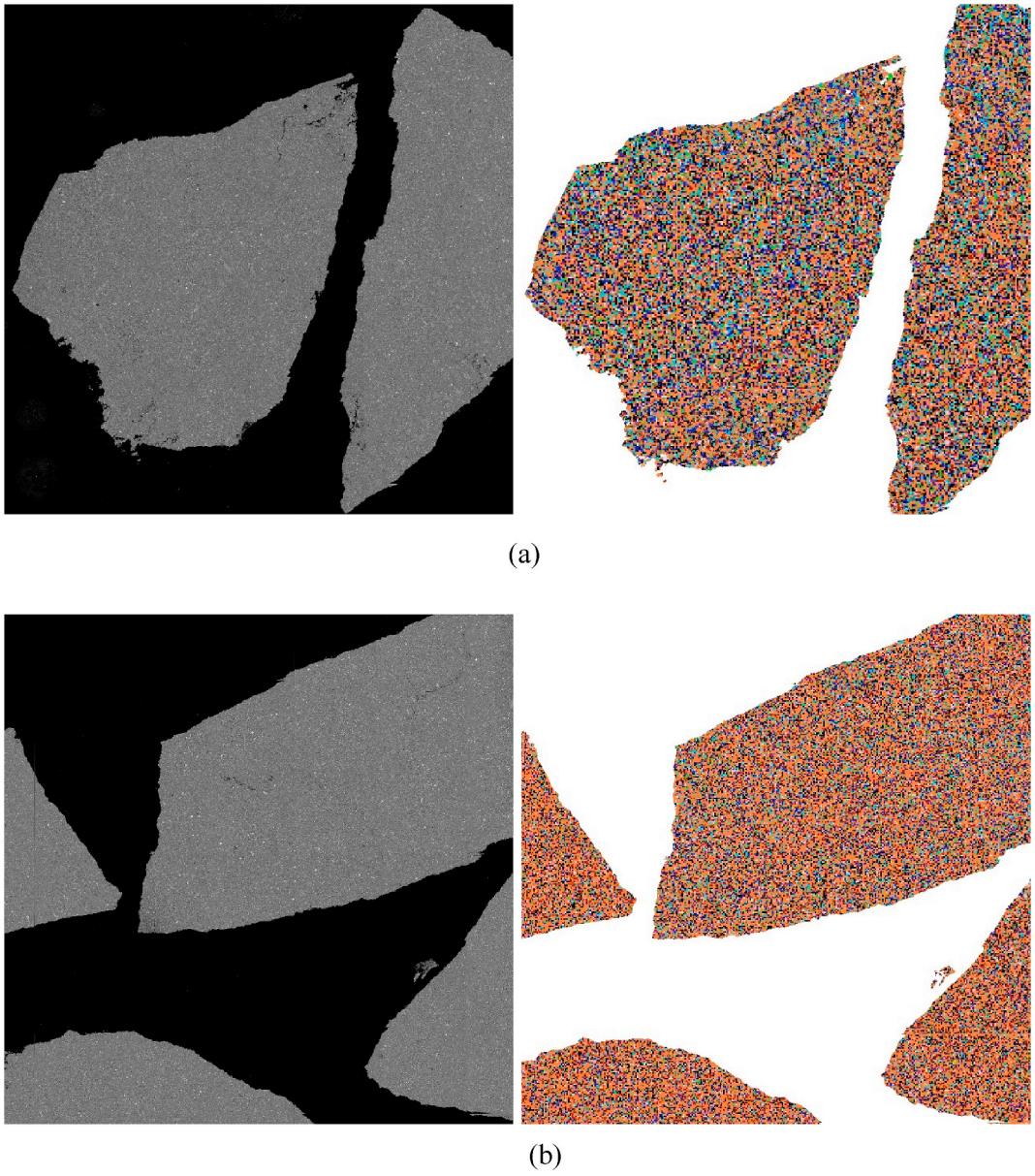

Fig. A2.1. Typical SEM-MLA data for (a) U1, (b), U2, (c), U3, (d) U4 and (e) (U5).

(a) U1 BSE and corresponding mineral map showing the clay sized particle matrix dominated by illite (orange) with interspersed grains of quartz (blue) and carbonate (turquoise).
(b) U2 BSE and corresponding mineral map demonstrating the same clay sized particle matrix dominated by illite (orange). Compared to U1 there are fewer carbonate (turquoise) grains, and they show no preferential alignment and/or distribution.
(c) U3 BSE and corresponding mineral map showing the presence of a clay sized grain matrix dominated by illite (orange) as well as grains of quartz (blue), however there is a significantly greater quantity of carbonates (turquoise) in comparison to U1 and U2. These carbonates are present as bands and also in biogenic forms.
(d) U4 BSE and corresponding mineral map showing the presence, but reduction in the clay sized illite (orange) dominated matrix, within this matrix there are some quartz grains (blue) but far fewer than can be seen for samples U1, U2 and U3. There is a significant quantity of carbonates (turquoise) which take on a biogenic form likely as a result of bioturbation.
(e) U5 BSE and corresponding mineral map showing a carbonate grain (turquoise), with some fine grained quartz (blue) within it. There are also some areas of dolomite (green) where some mineral alteration has occurred.

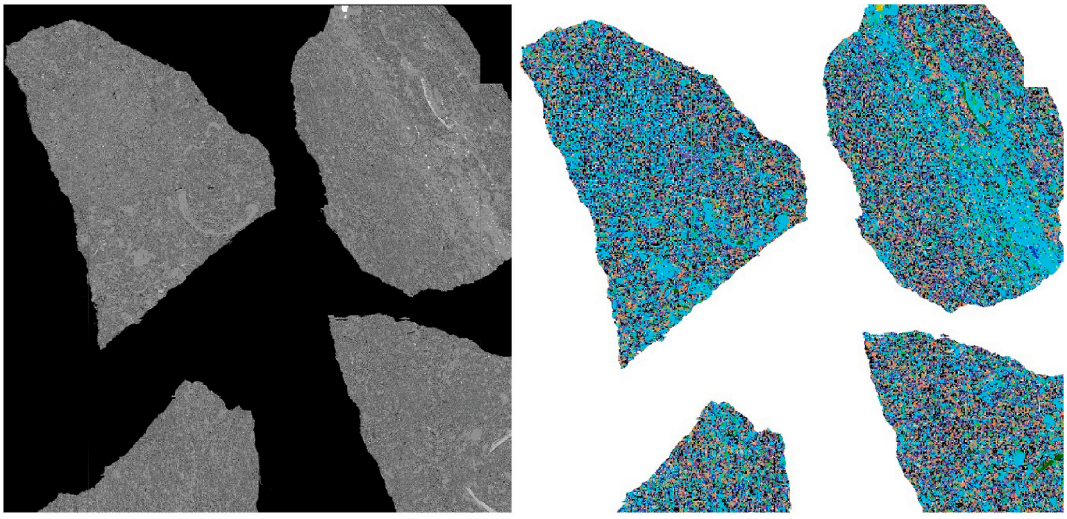

(c)

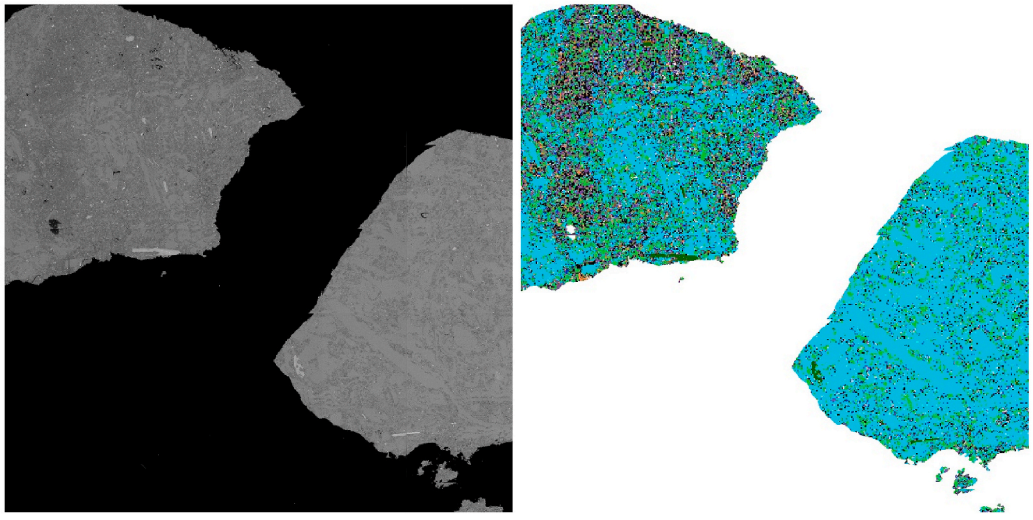

(d)

Fig. A2.1. (*continued*).

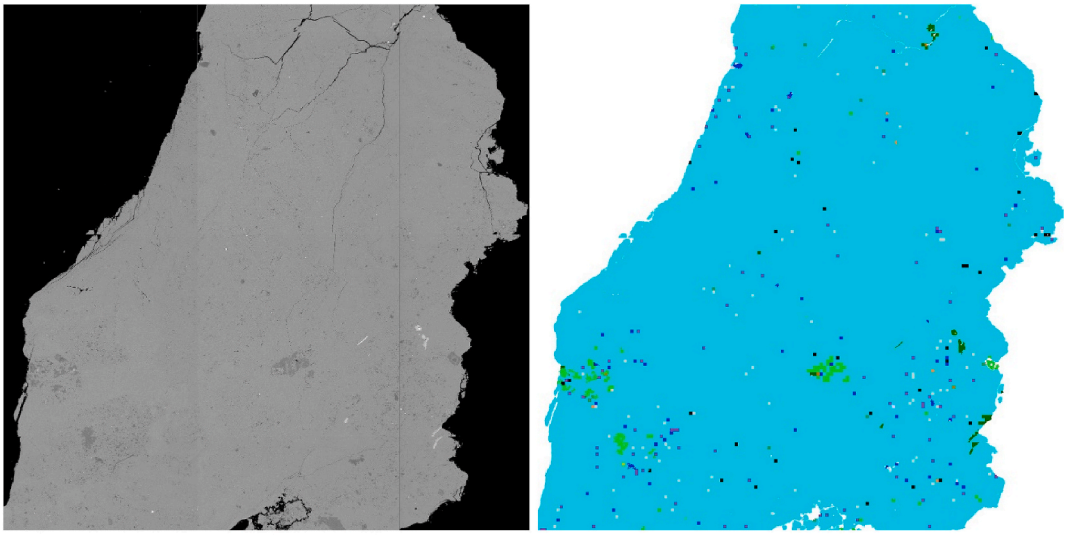

(e)

Fig. A2.1. (*continued*).

Appendix 3

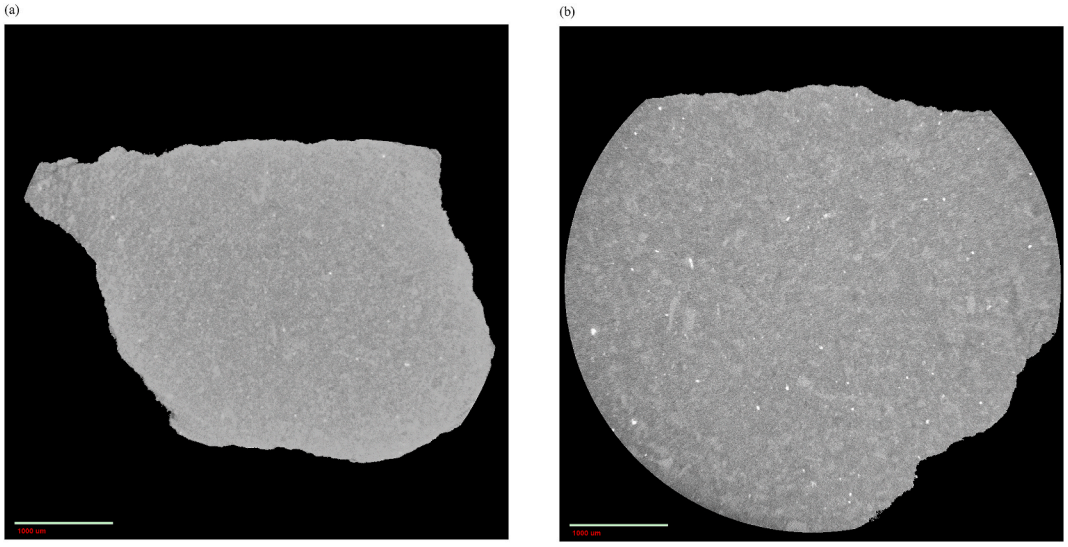

Fig. A3.1. Examples of reconstructed 2D slice CXT images of fresh samples of (a) U1 and (b) U3. The scale bar represents 1000 μm.

References

Ambegaokar, V., Halperin, B.I., Langer, J.S., 1971. Hopping conductivity in disordered systems. Phys. Rev. B 4, 2615–2620.
Aukett, P.N., Jessop, C.A., 1996. Assessment of connectivity in mixed meso/macroporous solids using nitrogen sorption. Fundamentals of Adsorption. Kluwer Academic Publishers, MA, pp. 59–66.
Barsotti, E., Tan, S.P., Piri, M., Chen, S.P., 2020. Capillary-condensation hysteresis in naturally-occurring nanoporous media. Fuel 463, 116441.
Brinkley, S.A., 2016. Petroleum Geology of the Utica/Point Pleasant Play in Washington County, Ohio. Master's Thesis, East Carolina University.
Broekhoff, J.C.P., De Boer, J.H., 1967. Studies on pore systems in catalysis X: calculations of pore distributions from the adsorption branch of nitrogen sorption isotherms in the case of open cylindrical pores. J. Catal. 9, 15–27.
Broekhoff, J.C.P., De Boer, J.H., 1968. Studies on pore systems in catalysis XIII: pore distributions from the desorption branch of a nitrogen sorption isotherm in the case of cylindrical pores. B. Applications. J. Catal. 10, 377–390.
Chen, Z., Song, Y., Jiang, Z., Liu, S., Li, Z., Shi, D., Yang, W., Yang, Y., Song, J., Gao, F., Zhang, K., Guo, X., 2019. Identification of organic matter components and organic pore characteristics of marine shale: a case study of Wufen-Longmaxi shale in southern Sichuan Basin, China. Mar. Petrol. Geol. 109, 56–69.
Cody, G.D., Davis, A., 1991. Direct imaging of coal pore space accessible to liquid metal. Energy Fuel. 5, 776–781.
Colton, G.W., 1961. Geologic Summary of the Appalachian Basin, with Reference to the Subsurface Disposal of Radioactive Waste Solutions. US Atomic Energy Comm. TEI-791.
Curtis, M.E., Cardott, B.J., Sondergeld, C.H., Rai, C.S., 2012. Development of organic porosity in the Woodford Shale with increasing thermal maturity. Int. J. Coal Geol. 103, 26–31.
Esparza, J.M., Ojeda, M.L., Campero, A., Dominguez, A., Kornhauser, I., Rojas, F., Vidales, A.M., Lopez, R.H., Zgrablich, G., 2004. N-2 sorption scanning behavior of SBA-15 porous substrates. Colloids Surf., A 241, 35–45.
Fandrich, R., et al., 2007. Modern SEM-based mineral liberation analysis. Int. J. Miner. Process. 84, 310–320.
Gregg, S.J., Sing, K.S.W., 1982. Adsorption, Surface Area and Porosity. Academic Press Inc, London.
Hickman, J., Eble, C., Riley, R.A., Erenpreiss, M., Carter, K.M., Harper, J.A., Dunst, B., Smith, L., Cooney, M.L., Soeder, D., Metzger, G., 2015. A geologic play book for Utica shale Appalachian Basin exploration. Appalachian Oil and Natural Gas

Research Consortium 2. https://researchrepository.wvu.edu/aongrc/2. (Accessed 3 December 2020). accessed.
Hitchcock, I., Malik, S., Holt, E.M., et al., 2014. Impact of chemical heterogeneity on the accuracy of pore size distributions in disordered solids. J. Phys. Chem. C 118, 20627–20638.
Jarvie, D.M., Hill, R.J., Pollastro, R.M., 2005. Assessment of the gas potential and yields from shales: the Barnett Shale model. Okla. Geol. Surv. Circ. 110 (2005), 37–50.
Ji, L., Jiang, W., Cao, G., Zhou, J., Luo, C., 2019. Investigation into the apparent permeability and gas-bearing property in typical organic pores in shale rocks. Mar. Petrol. Geol. 110, 871–885.
Katz, A.J., Thompson, A.H., 1986. Quantitative prediction of permeability in porous rock. Phys. Rev. B 34, 8179–8181.
Kaufmann, J., 2010. Pore space analysis of cement-based materials by combined nitrogen sorption – Wood's metal impregnation and multi-cycle mercury intrusion. Cement Concr. Compos. 32, 514.
Keller, L.M., Schuetz, P., Erni, R., Rossell, M.D., Lucas, F., Gasser, P., Holtzer, L., 2013. Characterization of multi-scale microstructural features in Opalinus clay. Microporous Mesoporous Mater. 170, 83–94.
Kim, T.H., Cho, J., Lee, K.S., 2017. Evaluation of CO2 injection in shale gas reservoirs with multi-component transport and geomechanical effects. Appl. Energy 190, 1195–1206.
Liu, D., Li, Y., Yang, S., Agarwal, R.K., 2019. CO2 sequestration with enhanced shale gas recovery. Energy Sources, Part A Recover. Util. Environ. Eff. https://doi.org/10.1080/15567036.2019.1587069.
Luft, S.J., 1971. Geologic map of part of the covington quadrangle, northern Kentucky: US geological Survey quadrangle map GQ-955, scale 1: 24,000. 1972. Geologic map of the butler quadrangle, pendleton and campbell counties, Kentucky: US geological Survey geologic quadrangle map GQ-982. scale 1 (24,000).
Ma, L., Taylor, K.G., Dowey, P.J., Courtois, L., Gholina, A., Lee, P.D., 2017. Multi-scale 3D characterisation of porosity and organic matter in shales with variable TOC content and thermal maturity: examples from the Lublin and Baltic Basins, Poland and Lithuania. Int. J. Coal Geol. 180, 100–112.
Ma, L., Dowey, P.J., Rutter, E., Taylor, K.G., Lee, P.D., 2019. A novel upscaling procedure for characterising heterogeneous shale porosity from nanometer-to millimetre-scale in 3D. Energy 181, 1285–1297.
Mahnke, M., Mögel, H.J., 2003. Fractal analysis of physical adsorption on material surfaces. Colloids Surf., A 216, 215–228.
MacDowell, R.C. (Ed.), 1986. The Geology of Kentucky: A Text to Accompany the Geologic Map of Kentucky; a Description of the Stratigraphic Units Shown on the State Geologic Map, with Discussions of the Structural Geology, Economic Geology, and Physiographie of the State. US Government Printing Office.
Murray, K.L., Seaton, N.A., Day, M.A., 1999. An adsorption-based method for the characterization of pore networks containing both mesopores and macropores. Langmuir 15, 6728–6737.
Nepryahin, A., Fletcher, R., Holt, E.M., Rigby, S.P., 2016a. Structure-transport relationships in disordered solids using integrated rate of gas sorption and mercury porosimetry. Chem. Eng. Sci. 152, 663–673.
Nepryahin, A., Fletcher, R., Holt, E.M., Rigby, S.P., 2016b. Techniques for direct experimental evaluation of structure-transport relationships in disordered porous solids. Adsorption 22, 993–1000.
Pfeifer, P., Avnir, D., 1983. Chemistry in noninteger dimensions between two and three. I. Fractal theory of heterogeneous surfaces. J. Chem. Phys. 79, 3558–3565.
Popova, O., 2017. Utica Shale Play-Geology Review. Independent Statistics & Analysis. Report, United States Energy Information Administration. US Department of Energy, Washington DC.
Rigby, S.P., 2018. Recent developments in the structural characterisation of disordered. Mesoporous Solids. JMTR 62, 296–312.
Rigby, S.P., 2020. Structural Characterisation of Natural and Industrial Porous Materials: A Manual. Springer International Publishing, Cham.
Rigby, S.P., Fletcher, R.S., Riley, S.N., 2004. Characterisation of porous solids using integrated nitrogen sorption and mercury porosimetry. Chem. Eng. Sci. 59, 41–51.
Rigby, S.P., Jahan, H., Stevens, L., Uguna, C., Snape, C., Macnaughton, B., Large, D.J., Fletcher, R.S., 2020. Pore structural evolution of shale following thermochemical treatment. Mar. Petrol. Geol. 112, 104058.
Rouquerol, F., Rouquerol, J., Sing, K., 1999. Adsorption by Powders and Porous Solids: Principles, Methodology and Applications. Academic Press, London.
Saif, T., Lin, Q., Butcher, A.R., Bijeljic Blunt, M., 2017. Multi-scale multi-dimensional microstructure imaging of oil shale pyrolysis using X-ray micro-tomography, automated ultra-high resolution SEM, MAPS mineralogy and FIB-SEM. Appl. Energy 202, 628–647.
Sang, G., Liu, S., Elsworth, D., Yang, Y., Fan, L., 2020. Evaluation and modeling of water vapor sorption and transport in nanoporous shale. Int. J. Coal Geol. 228, 103553.
Seaton, N.A., 1991. Determination of the connectivity of porous solids from nitrogen sorption measurements. Chem. Eng. Sci. 46, 1895–1909.
Seaton, N.A., Friedman, S.P., MacElroy, J.M.D., Murphy, B.J., 1997. The molecular sieving mechanism in carbon molecular sieves: a molecular dynamics and critical path analysis. Langmuir 13, 1199–1204.
Seemann, T., Bertier, P., Krooss, B.M., Stanjek, H., 2017. Water vapour sorption on mudrocks. In: Geomechanical and Petrophysical Properties of Mudrocks, vol. 454. Geological Society, London, Special Publications, pp. 201–234.
Shiko, E., Edler, K.J., Lowe, J.P., Rigby, S.P., 2012. Probing the impact of advanced melting and advanced adsorption phenomena on the accuracy of pore size distributions from cryoporometry and adsorption using NMR relaxometry and diffusometry. J. Colloid Interface Sci. 385, 183–192.
Smith, L.B., 2013. August. Shallow transgressive onlap model for Ordovician and Devonian organic-rich shales, New York State. In: Unconventional Resources Technology Conference. Society of Exploration Geophysicists, American Association of Petroleum Geologists, Society of Petroleum Engineers, pp. 524–533.
Spanakos, D., Rigby, S.P., 2020. Predicting surface diffusivities of gas molecules in shale. Energy Fuels 34, 12417–12428.
Swapp, S., 2017. Scanning Electron Microscopy (SEM). University of Wyoming.
Sylvester, P.J., 2012. 'Use of the Mineral Liberation Analyzer (MLA) for Mineralogical Studies of Sediments and Sedimentary Rocks', Quantitative Mineralogy and Microanalysis of Sediments and Sedimentary Rocks. Mineralogi(May), pp. 1–16.
Tompsett, G.A., Krogh, L., Griffin, D.W., Conner, W.C., 2005. Hysteresis and Scanning Behavior of Mesoporous Molecular Sieves 21, 8214–8225.
Walker, W.C., Zettlemoyer, A.C., 1948. A dual-surface BET adsorption theory. Y. Phys. Colloid Chem. 52, 47–58.
Wang, R., Sang, S., Zhu, D., Liu, S., Yu, K., 2018. Pore characteristics and controlling factors of the lower cambrian hetang Formation shale in northeast jiangxi, China. Energy Explor. Exploit. 36, 43–65.
Wardlaw, N.C., McKellar, M., 1981. Mercury porosimetry and the interpretation of pore geometry in sedimentary rocks and artificial models. Powder Technol. 29, 127–143.
Wickstrom, L.H., Riley, R., Erenpreiss, M., Perry, C., 2013. Geologic Overview and Activity Update for the Utica-Point Pleasant Shale Play in Ohio. http://www.searchanddiscovery.com/documents/2012/10409wickstrom/ndx_wickstrom.pdf. (Accessed 4 December 2020). accessed.